Journal of Hydrology 663 (2025) 134013

Contents lists available at ScienceDirect

Journal of Hydrology

journal homepage: www.elsevier.com/locate/jhydrol

Research papers

Chained hydrologic-hydraulic for flood modeling by assimilating SAR-derived flood extent and FFSAR-processed altimetry data

Thanh Huy Nguyen [a,*], Sophie Ricci [b,c], François Boy [d], Andrea Piacentini [b], Simon Munier [e], Santiago Peña Luque [d], Christophe Fatras [f], Ludovic Cassan [b,c], Raquel Rodriguez Suquet [d]

[a] LIST (Luxembourg Institute of Science and Technology), 4362 Esch-sur-Alzette, Luxembourg
[b] CERFACS (Centre Européen de Recherche et de Formation Avancée en Calcul Scientifique), 31057 Toulouse Cedex 1, France
[c] CECI, Univ. Toulouse, CERFACS/CNRS/IRD, 31057 Toulouse Cedex 1, France
[d] CNES (Centre National d'Études Spatiales), 31401 Toulouse Cedex 9, France
[e] Météo-France, CNRS, Univ. Toulouse, CNRM (Centre National de Recherches Météorologiques), 31057 Toulouse Cedex 1, France
[f] CLS (Collecte Localisation Satellites), 31520 Ramonville-Saint-Agne, France

ARTICLE INFO

This manuscript was handled by Emmanouil Anagnostou, Editor-in-Chief, with the assistance of Xinyi Shen, Associate Editor.

Keywords:
Flooding
Hydrodynamics
Data assimilation
Altimetry
Sentinel-6
Fully-focused SAR

ABSTRACT

Flood inundation mapping for gauged and ungauged basins relies on chained hydrologic-hydrodynamic models, combined with multi-source remote sensing (RS) datasets and in-situ gauge measurements when available. In this work, a large-scale hydrologic model provides forcing data to a high-fidelity local hydrodynamic model. The latter acts as an advanced interpolator, bridging the gap in both space and time between the high-frequency yet sparse in-situ measurements and the large-coverage but less frequent satellite data gathered from various Earth Observation (EO) missions. These data are combined with physics-based equations using data assimilation (DA) algorithms. This study presents a novel use of nadir and off-nadir altimetry data from the Sentinel-6 (S6) mission, processed with Fully-focused SAR (FFSAR) algorithms, alongside Sentinel-1 (S1) SAR-derived flood extents, for DA over the Garonne River. Using a dual state-parameter Ensemble Kalman Filter (EnKF), it is shown that assimilating S6 altimetry data brings significant improvements along the riverbed, as well as addressing gaps left by other remote sensing datasets. It was demonstrated that DA allows for the combination of various EO datasets, overcoming the limitations of spatial RS low-revisit frequency and improving the representation of the flood dynamics in the riverbed and the floodplains.

1. Introduction

Major devastating floods have been occurring around the world, with an increased intensity in the last decade, exacerbated by global climate change (Masson-Delmotte et al., 2021a,b). For instance, Wasko et al. (2021) found that extreme rainfall has become more frequent, with shorter storm events and reduced frequent flood peaks, but an increase in rarer flood peaks due to shifts in soil moisture. On the other hand, Boulange et al. (2021) emphasize the important role of dams in mitigating global flood risk under climate changes. Flooding alone is responsible for approximately 40% of all natural disasters globally (Shah et al., 2018; United Nations Office for Disaster Risk Reduction, 2020, 2022); Up to 1.47 billion people are directly at risk of flooding (Rentschler and Salhab, 2020). Flood damages have indeed increased in recent years, driven by climate-related changes and rising asset values in flood-prone areas (Blöschl et al., 2019). Hence, monitoring and predicting floods holds paramount importance, operating in both hindcast and forecast modes (Jamali et al., 2018; Pinter et al., 2017; Begg, 2018).

1.1. Role of Earth Observation data in flood monitoring and forecasting

Early flood warning and emergency management systems rely on the synergy between high-fidelity numerical models and dense, reliable observing networks. Due to the global decline of in-situ gauge data (The Ad Hoc Group et al., 2001), the role of remote sensing (RS) data is becoming increasingly important. Indeed, flood management has been assisted by an increasing amount of data from satellite Earth Observation (EO) missions, providing heterogeneous and relevant satellite data, namely altimetry, optical and synthetic aperture radar (SAR). The

* Corresponding author.
E-mail address: thanh-huy.nguyen@list.lu (T.H. Nguyen).

https://doi.org/10.1016/j.jhydrol.2025.134013
Received 19 July 2024; Received in revised form 27 June 2025; Accepted 31 July 2025
Available online 23 August 2025

integration of RS observations into hydrodynamic models significantly improves the flood reanalysis and forecasting capabilities. These include Digital Elevation Model (DEM), river dimensions, WLs, flow rates, and flood extents. In addition, EO data not only provides insights into the physical aspects of floods, i.e. their extent and surface elevation, but also offers highly impactful socioeconomic data (Annis and Nardi, 2019). This added dimension improves our understanding of vulnerability and facilitates damage assessment, ultimately strengthening our capacity to mitigate risks (Adeel et al., 2020).

Satellite radar altimetry stands out as a valuable technology for monitoring water surface elevations (WSEs) and river discharge from space. Schumann et al. (2023) provided a comprehensive review and discussed the great potential for enhanced mapping and monitoring of floods using RS data, including satellite radar altimetry. Its significance extends to hydrology studies, particularly those associated with remote or poorly-gauged catchments (Jarihani et al., 2013; Domeneghetti, 2016), thanks to global scale and high spatial coverage. This encompasses both nadir and large-swath radar altimeters. Research into satellite altimetry for river monitoring spans a spectrum of climates, namely in Arctic, temperate and/or tropical climates (Da Silva et al., 2010; Biancamaria et al., 2017), as well as extending across various rivers and river basins, such as the Amazon (Da Silva et al., 2010) and the Mekong (Chang et al., 2019; Boergens et al., 2017), as well as relatively small ones (Sulistioadi et al., 2015; Bogning et al., 2018). More technical details on satellite radar altimetry can be found in Appendix A.

Jiang et al. (2019) carried out a simultaneous calibration of hydrodynamic models, focusing on Strickler's friction coefficients and river datum, using various altimetry data. Their findings suggested that for calibrating parameters in large-scale river hydrodynamic models, spatial resolution holds greater significance than temporal resolution and observation accuracy. Notably, CryoSat-2 demonstrated superior performance compared to other altimeters such as SARAL, Jason-1, and Jason-2 in identifying said parameters. Similarly, Brêda et al. (2019) conducted an estimation of river bathymetry by assimilating various satellite altimetry missions, analyzing real data from ENVISAT, ICESat, and Jason-2, along with synthetic altimetry data from ICESat-2, Jason-3, SARAL, and SWOT. As such, they asserted that the bathymetry estimation performance depends strongly on the satellite inter-track distance, since a greater number of observation sites leads to better estimates.

The large-swath Surface Water and Ocean Topography (SWOT) altimeter was launched in 2022. Equipped with a Ka-band Radar Interferometer (KaRIn), it aims to provide sea surface heights and continental WSE maps globally with a 21-day revisit frequency, covering a 120-km wide swath (with an approximately 20-km gap at the nadir track). The merits of SWOT-derived river products for the estimation of discharge were recently demonstrated in Wongchuig-Correa et al. (2020), Durand et al. (2023). Nevertheless, the major drawback of altimetry data in hydrology is still the low temporal resolution, especially in the context of flood monitoring and forecasting. Recent advancements have addressed this challenge by combining multiple satellite altimetry missions (Boergens et al., 2017; Tourian et al., 2016; Zakharova et al., 2020). In this paper, we combine flood observations from multiple EO data sources, including in-situ data, Sentinel-1 (S1) SAR flood extent and Sentinel-6 (S6) WSE measurements processed with Fully-focused SAR (FFSAR) (Egido and Smith, 2016).

Water bodies and flooded areas typically show low backscatter on SAR images, as radar pulses are mostly reflected away from the sensor when they hit smooth water surfaces (Martinis et al., 2015). S1 is equipped with a C-band SAR system operating at a frequency of 5.405 GHz (Torres et al., 2012), making it well-suited for such applications. Two polar-orbiting identical satellites work as a constellation allowing a six-day repeat cycle. They were launched respectively on 2014-04-03 and 2016-04-26. However, since 2021-12-23, S-1B became defective due to a technical anomaly, this led to a lack of global SAR imagery, which had been typically useful for flood monitoring. The need for other RS datasets thus becomes all the more necessary in order to monitor floods from space. In this work, we investigate how altimetry data from the S6 mission, including off-nadir observations, with FFSAR processing (Egido and Smith, 2016) can participate in this effort.

The FFSAR (Egido and Smith, 2016) processing technique allows to achieve high resolution and accuracy of nadir altimetry data, by performing fully-focused coherent processing of pulse echoes from a nadir-looking pulse-limited radar altimeter. Kleinherenbrink et al. (2018) presented an application of FFSAR on the CryoSat-2 altimetry in the Wadden Sea, discussing its potential utility in monitoring water surface dynamics in this coastal environment, whereas Molina Burgués et al. (2023) investigated the merits of extracting WSEs measurements using S6 FFSAR, with a focus on inland targets including relatively small reservoirs and lakes, compared to in-situ data. Gómez Olivé et al. (2023) studied water extent measurements using S6 FFSAR data, aiming to assess its effectiveness in delineating water bodies against optical (Sentinel-2) measurements and in-situ observations.

1.2. Improving flood prediction with data assimilation

A recent review by Jafarzadegan et al. (2023) provides a comprehensive flood forecasting framework and recommendations to improve forecasting systems. It advocates for the development of an integrated modeling platform with data assimilation (DA), which articulates the interaction among all of the Earth components, taking into account the chain of uncertainties with an ensemble-based approach in order to provide flood inundation mapping capabilities. Hydrologic and hydrodynamic numerical models play a central role in representing and predicting flood discharge and water levels (WLs) in the river mainstream as well as in the floodplain. As such, coupling hydrologic and hydrodynamic models is commonly employed in flood forecasting systems. This approach is crucial for ensuring precise predictions of flood extents and water depths across expansive catchments, essential for effective flood management (Grimaldi et al., 2016). Nevertheless, their effectiveness is hampered by the inherent uncertainties present in their input data. In this regard, DA has been demonstrated to be highly efficient in hydrology studies to reduce such uncertainties. It combines numerical models with observations from in-situ stream gauges and from satellite EO (Mason et al., 2012; Hostache et al., 2018).

The assimilation of RS-derived WSE is advantageous as it directly uses a key diagnostic variable of the model (Giustarini et al., 2011; Annis et al., 2022). Revilla-Romero et al. (2016) assimilated the Global Flood Detection System's daily surface water extents with an Ensemble Kalman Filter (EnKF) to improve streamflow forecasts in Africa and South America. Despite the coarse spatial resolution of their results (i.e. $0.1° \times 0.1°$), the EnKF updated simulated groundwater levels using innovations in streamflow volumes, significantly enhancing flood peak predictions in ungauged catchments. Other studies on DA into hydraulic models or forecasting systems integrate synthetic, in situ or RS-derived WLs, such as Annis et al. (2022) with EnKF, and García-Pintado et al. (2013, 2015), Andreadis and Schumann (2014) with Ensemble Transform Kalman Filters (ETKF). Lai et al. (2014) implemented a 4D-Var DA scheme, integrating MODIS-derived flood extents into a 2D Shallow Water model to improve roughness parameter estimates in floodplains. Using SAR images, flood probability maps have been estimated (Giustarini et al., 2016) and assimilated into a Particle Filter (PF) framework (Hostache et al., 2018; Dasgupta et al., 2021; Di Mauro et al., 2021) built on top of a cascade hydrologic–hydraulic model (i.e. SUPERFLEX (Fenicia et al., 2011) and LISFLOOD-FP (Bates and De Roo, 2000)), where particles were weighted by their fit with the SAR observations. Di Mauro et al. (2021) introduced a tempering coefficient to reduce PF degeneracy and enhance forecasts.

1.3. Objective and outline

This study focuses on reducing uncertainties in hydrodynamic model parameters, forcing data, and hydraulic state variables to improve the overall flood prediction in hindcast mode. This is achieved through the joint assimilation of the S1-derived flood observations and the high-spatial density altimetry data from S6. It builds upon previous work by Nguyen et al. (2022b, 2023b), Ricci et al. (2023), using the TELEMAC-2D[1] (T2D) hydrodynamic model over the Garonne Marmandaise catchment in southwestern France. While Nguyen et al. (2022b) proposed the assimilation of wet surface ratios (WSR) derived from S1 observed flood extent maps using a dual state-parameter EnKF scheme Moradkhani et al. (2005), andNguyen et al. (2023b) later extended this by addressing the non-Gaussian nature of these observations through anamorphosis, both studies were limited to uncertainties in observed inflow discharges. Similarly, preliminary work (Ricci et al., 2023) was carried out to validate 1D and 2D hydraulic MASCARET-TELEMAC models using S6-derived data. In contrast, the current work further assimilates S6 FFSAR-processed data and deals with highly uncertain discharges produced by the large-scale hydrological model ISBA-CTRIP. The WSR computes the ratio of wet pixels detected on SAR S1-derived flood extent maps over the total number of pixels within each subdomain of the floodplain. In the present work, S6 altimetry data have been processed with FFSAR (Egido and Smith, 2016; Boy et al., 2023) to provide a spatially dense profile of WSE every 10 m along the river centerline at each overpass time. T2D is forced by the ISBA-CTRIP hydrologic model (Decharme et al., 2019; Munier and Decharme, 2022) to allow for ungauged catchment study and increased forecast lead times beyond the transfer time of the hydraulic network (Nguyen et al., 2023a; Nguyen et al., 2024).

The remainder of the article is organized as follows. Section 2 presents the hydrologic and hydrodynamic models, whereas Section 3 describes the EO data and the processing algorithms. The DA strategy and experimental settings are detailed in Section 4. Section 5 discusses the merits of the multi-source DA with comprehensive assessments in the control space and the observation space. Finally, conclusions and perspectives are summarized in Section 6.

2. Chained hydrologic-hydrodynamic models

2.1. The Garonne Marmandaise hydrodynamic model

The study area involves a reach of the Garonne River between Tonneins and La Réole (southwest of France) focusing on an overflowing event that occurred between December 2021 and February 2022. In the 19th century, this section of the valley was fortified with flood protection infrastructure following the devastating 1875 Garonne flood. A network of dykes and weirs was gradually developed to safeguard the floodplains, manage submersion areas, and enhance flood retention, protecting local residents from future flooding events. This presents an opportunity for DA to correct the uncertainties related to the hydrodynamic model's parameters and inputs. In addition, the catchment is large enough to be modeled by the large-scale hydrologic model ISBA-CTRIP. The Garonne River is also one of the sites that are regularly observed by multiple satellite missions. Over this reach depicted in Fig. 1, a T2D hydrodynamic numerical model (Hervouet, 2007) was developed and calibrated by Laboratoire National d'Hydraulique et Environnement (LNHE, EDF R&D) (Besnard and Goutal, 2011). It was constructed on a mesh of over 40,000 nodes based on existing bathymetric cross-sectional surveys and topographic data (Besnard and Goutal, 2011). Given a forcing inflow discharge at Tonneins and a downstream rating curve at La Réole, the T2D model simulates the water level and velocity at every node of the mesh. Previous works (Nguyen et al., 2022b,a) have described in detail the T2D hydrodynamic model set up to simulate the dynamics of the flow, as well as two major flood cases in 2019 and 2021. In this catchment, three in-situ observing stations are traditionally operated by the VigiCrue[2] network at Tonneins, Marmande, and La Réole, and two others at Couthures-sur-Garonne (installed on 2021-02-18) and Mas d'Agenais (installed on 2022-11-26) managed by Vortex-io.[3] They are represented by the black solid circles in Fig. 1. The studied flood event from December 2021 to February 2022 peaked at a discharge of 4,800 $m^{1/3}\ s^{-1}$ on January 12, 2022, nearly reaching the 5-year flood return period at Tonneins (i.e. 4,860 $m^{1/3}\ s^{-1}$).

Table 1
Statistics for the PDF of friction parameters, corrective coefficient to the upstream discharge and WL correction in floodplain subdomains, assuming Gaussian laws.

Parameter	Calibrated/ default values $\mathbf{x}_0$	Standard deviation $\sigma_{\mathbf{x}}$	95% confidence interval
K_{s_0}	17 [$m^{1/3}\ s^{-1}$]	0.85	17 ± 1.67
K_{s_1}	45 [$m^{1/3}\ s^{-1}$]	2.25	45 ± 4.41
K_{s_2}, K_{s_3}	38 [$m^{1/3}\ s^{-1}$]	1.9	38 ± 3.72
$K_{s_4}, K_{s_5}, K_{s_6}$	40 [$m^{1/3}\ s^{-1}$]	2.0	40 ± 3.92
μ	1 [−]	0.06	1 ± 0.118
γ	0 [s]	900	0 ± 1763.97
$\delta H_k\ (k \in [1,5])$	0 [m]	0.25	0 ± 0.49

The main sources of uncertainties are inherent in the friction coefficients of the riverbed and floodplain, prior hydrologic forcing conditions, and the hydraulic state within subdomains of the floodplain. Friction coefficients include one Strickler coefficient in the floodplain (K_{s_0}) and six others in the riverbed (K_{s_1} to K_{s_6}). Upstream forcing $Q(t)$ undergoes correction via a multiplicative factor μ and a time shift γ, so that $Q_{posterior}(t) = \mu \times Q_{prior}(t-\gamma)$. El Garroussi et al. (2022, 2019) carried out several sensitivity analyses over this catchment using the same hydrodynamic model. It is shown that the inflow discharge is responsible for 80% of the WL variances over the whole domain, while the Strickler coefficients are important to the WL in the riverbed. Lastly, the hydraulic state within five floodplain subdomains is adjusted with WL additive increments across the subdomains (denoted by δH_1 to δH_5), as depicted by hatched regions in Fig. 1. Such correction accounts for the lack of representation of evapotranspiration and ground infiltration processes in the hydrodynamic model. The prior values for these random variables are summarized by Table 1. They follow Gaussian distributions and are used for the ensemble generation. The calibrated values of friction coefficients (K_{s_0} to K_{s_6}) were obtained from the initial calibration (Besnard and Goutal, 2011). They are used for the generation of the ensemble at the first cycle. The floodplain roughness has typically low sensitivity, as its dynamics is mainly controlled by hydraulic structures (i.e. dykes, culvert passage, secondary hydrographic network) and here it is corrected by the DA with δH. The study is carried out over a lengthy period of 78 days between 2021-11-30 and 2022-02-15.

2.2. Large-scale ISBA-CTRIP model

The large-scale hydrologic model ISBA-CTRIP integrates the ISBA (Interaction Sol-Biosphère-Atmosphère) land surface model (Noilhan and Planton, 1989) and the CNRM-modified version of the TRIP (Total Runoff Integrating Pathways) river routing model (RRM) (Oki and Sud, 1998). While ISBA simulates heat and water balance exchanges at the soil-atmosphere-vegetation interfaces and handles hydrological processes such as surface and deep runoff, CTRIP focuses on the lateral transfer of freshwater down towards the continent-ocean interface.

[1] www.opentelemac.org

[2] https://www.vigicrues.gouv.fr/

[3] https://www.vortex-io.fr/

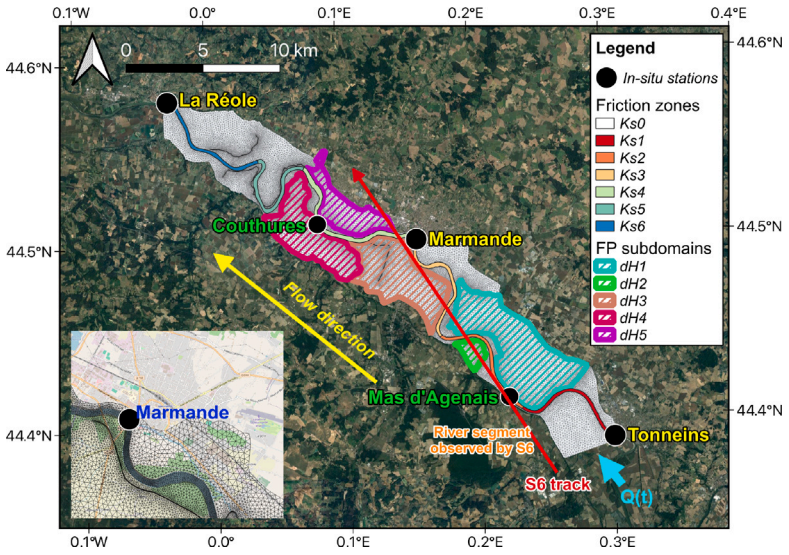

Fig. 1. T2D model on the Garonne at Marmande. Black solid dots represent in-situ observing stations. Friction zones in the riverbed are colored. Five subdomains of the floodplain are delineated and represented by hatched regions. The inset (bottom left) shows Marmande urban area. (Map data: © Google, Maxar Technologies.). (For interpretation of the references to color in this figure legend, the reader is referred to the web version of this article.)

ISBA operates on a global scale with a $0.5° \times 0.5°$ regular grid. The energy and water budget over continental surfaces are formulated on such a grid, incorporating a three-layer soil structure. ISBA provides a diagnosis of the surface runoff and the gravitational drainage (i.e., water percolating to the deep layers of the soil). They are subsequently used as forcing inputs for CTRIP. On the other hand, CTRIP is defined on a regular latitude-longitude grid at $1/12°$ resolution (Decharme et al., 2019, 2012; Munier and Decharme, 2022). It facilitates water transfer (laterally from one cell to another) along a river network down to the interface with the ocean, generating spatially distributed discharge maps. Uncertainties in the simulated discharges mainly stem from uncertainties in the land surface model inputs (i.e., precipitation), RRM parameters and catchment descriptions. The ISBA-CTRIP discharge time-series used as forcing for the T2D model has an hourly timestep.

Fig. 2 displays the discharge times-series at Tonneins (the prior upstream BC $Q_{prior}(t)$) simulated by ISBA-CTRIP (blue), in comparison to the observed discharge (orange) at the VigiCrue in-situ station. Performance metrics indicate a Nash–Sutcliffe Efficiency (NSE) of 0.65 and a root mean square error (RMSE) of 597.2 $m^3\ s^{-1}$, reflecting a significant underestimation of discharge by ISBA-CTRIP, compared to the observed discharge. S6 (respectively, S-1A/1-B) overpass times are indicated with cyan (respectively, yellow/gray) vertical lines. It appears that ISBA-CTRIP mostly underestimates the discharge, especially near the peaks, with shortened high-flow periods. It should also be noted that the simulated discharge also slightly overestimates low flows between 2022-01-02 and 2022-01-09, and after 2022-02-01.

3. Data and Data processing algorithms

3.1. In-situ data

Observing in-situ stations operated by the VigiCrue network, providing WL time-series, are available at Tonneins, Marmande, and La Réole (black solid circles in Fig. 1). Following a major flooding event in early 2021, another station was installed by Vortex-io at Couthures-sur-Garonne (referred to as Couthures). The present study focuses on a flood event that occurred in December 2021–February 2022. The in-situ WL measurements available every 15 min during this flood event at Tonneins (blue line), Marmande (orange line), and La Réole (green line), and at Couthures (cyan line), are displayed in Fig. 3. S6 (respectively, S-1A/-1B) overpass times are indicated with cyan (respectively, green/gray) vertical dashed and dotted lines. Here, it can be seen that S-1B became unavailable midway through the flood event. In this work, the in-situ WL time-series from the VigiCrue network, at Tonneins, Marmande, and La Réole, are used as assimilated data, whereas the WL time-series at the Couthures station are utilized solely as independent validation data.

3.2. Remote sensing data

SAR data, especially from the S1 constellation, offers significant advantages in flood studies due to its capability for all-day global mapping of continental water bodies and flooded areas almost regardless of weather conditions. In this study, the Interferometric Wide mode of S1 SAR is employed, featuring a ground resolution of 20×22 m with a 250-km swath. The data is then processed by resampling, reprojecting and distributing at 10×10 m for the Ground Range Detected at High resolution (GRDH) products. These S1 products are utilized to generate binary water maps using a Random Forest classification (Pal, 2005), developed within the FloodML[4] software (Huang et al., 2020; Kettig et al., 2021). Additional details are available in Nguyen et al. (2021, 2022a).

During the studied event of 78 days, a total of 26 S1 overpasses occurred across three orbits (ascending 30, ascending 132, and descending 8). Out of these, 21 images were captured by S-1A, while S-1B acquired five images. However, it should be noted that none of these images could have observed an overflowing in the floodplain. At the S1 overpass times, the WLs at Tonneins and Marmande were at most 10.40 m and 6.89 m, respectively—both below the reference overflow WLs of 11.07 m and 7.60 m, which correspond to the orange/amber risk threshold at these stations. However, in reality, on 2022-01-12, the peak in-situ WLs during the event reached 12.08 m at Tonneins and 8.78 m at Marmande, indicating overflow that was not detected by remote sensing data.

S6 is a Copernicus mission dedicated to monitoring Earth's oceans with unparalleled precision (Donlon et al., 2021). Through state-of-the-art radar altimeter technology, S6 delivers vital data on sea level rise, ocean circulation, and climate variability, crucial for understanding and

[4] https://github.com/CNES/floodml

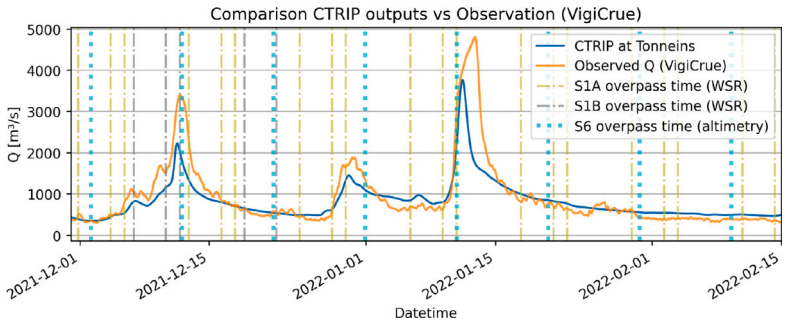

Fig. 2. Forcing data at Tonneins provided by ISBA-CTRIP discharge (blue), compared to observed discharge from VigiCrue station (orange). Vertical dash-dotted lines indicate S-1A (yellow) and S-1B (gray) overpass times whereas cyan dotted lines represent S6 overpass times. (For interpretation of the references to color in this figure legend, the reader is referred to the web version of this article.)

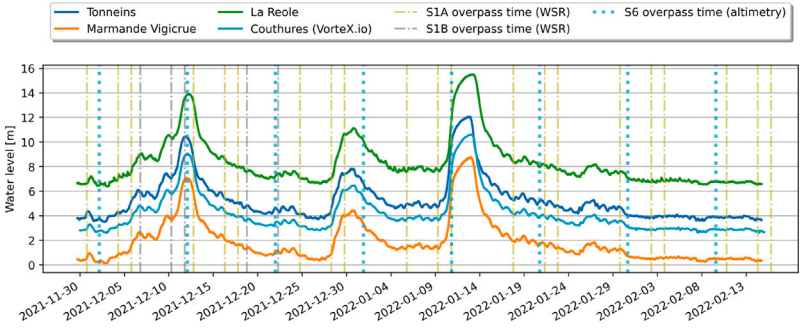

Fig. 3. Water level (H) time-series at Tonneins, Marmande, La Réole and Couthures, for the 2021–2022 flood event, in blue, orange, green and cyan respectively. Vertical dash-dotted lines show S-1A (yellow) and S-1B (gray) overpass times. Cyan dotted lines show S6 overpass times. (For interpretation of the references to color in this figure legend, the reader is referred to the web version of this article.)

mitigating the impacts of climate change. Beyond this main mission objective, S6 also provides very high-quality observations in continental hydrology. Launched on 2020-11-21, the S6 Michael Freilich satellite carries onboard a Ku/C-band nadir-pointing SAR altimeter, Poseidon-4, as well as a multi-frequency Advanced Microwave Radiometer for Climate (AMR-C) including an experimental High-Resolution Microwave Radiometer (HRMR). It aims to provide high accuracy altimetry measurements, namely Sea Surface Height from the range measurements, as well as wind speed and Significant Wave Height derived from normalized radar cross section. Using FFSAR processing applied on the S6 nadir data, the water surface elevation (WSE) over a segment of the Garonne River can be reconstructed (cyan dotted lines in Figs. 2 and 3) with a high along-track resolution (10 m). The S6 track over the Garonne River is represented by the red arrow in Fig. 1.

3.3. Algorithm for S6-derived WSE observations

The Poseidon-4 is the first radar altimeter to integrate a High-Resolution mode with an interleaved chronogram (Dinardo et al., 2024). Applied to these measurements, the FFSAR processing technique (Egido and Smith, 2016) delivers unprecedented precision in nadir altimetry for height measurements over rivers and lakes. Fig. 4 illustrates the radargram of the Poseidon-4 altimeter above the Garonne River in the Marmande sector (highlighted within the yellow rectangle), processed in FFSAR mode to achieve a metric resolution with a posting rate of the same order of magnitude.

The robust signal-to-noise-ratio (SNR) exceeding 20 dB enables clear identification of the river profile and geometry within the radar echoes, as shown in Fig. 4. Here, the Garonne River flows along the satellite track (as shown in Fig. 1), and although the water body is not always located under the nadir of the radar, CNES has developed an innovative processing technique to exploit both nadir and off-nadir signals in order to estimate a longitudinal profile of water heights (Boy et al., 2023). Such an approach by Boy et al. (2023) is not universally applicable, with several constraints limiting its effectiveness. Notably, the river's deviation from the satellite track should not exceed 2 km (in along-track distance) to avoid significant degradation in off-nadir observation errors. Nevertheless, in the studied sector of Garonne Marmandaise, this technique proves applicable and delivers exceptional performance (see Fig. 6).

The algorithm first involves isolating the echoes resulting from the reflection of the radar microwave signals by the river. To accomplish this, a centerline of the river was used, which facilitates the identification of the river's geometry within the radargram. Once these signals are identified and isolated, similar processing techniques employed in the operational ground segment are applied to the radar echoes in order to derive water heights. However, it is crucial to apply an additional correction known as the slant range correction to account for oblique sighting when the river is observed at a slight angle off-nadir. Fig. 5 illustrates the processing principle with the radargram obtained on 2022-02-09, and the WSE longitudinal profile obtained on the Garonne over 18-km length with a 10-m posting rate (i.e. ground spacing in the data). A similar method has been proposed by Ehlers et al. (2024, 2025) which is highly comparable to the WSE estimation algorithm (Boy et al., 2023) performed in this paper. It could serve as a suitable alternative, offering similar performance under comparable conditions.

This processing was validated by comparing the derived WSE estimates to several heterogeneous datasets. Firstly, the longitudinal profiles were compared to the VigiCrue station measurements located in Marmande, and to the Vortex-io station measurements in Mas d'Agenais. The measurement point closest to the Marmande station is approximately 700 m off-nadir. The agreement between the WSEs resulting from the algorithm and those observed by the in-situ station is excellent. This is evidenced by a Root Mean Square Error (RMSE) of 3.8 cm and 5.5 cm for Marmande and Mas d'Agenais, respectively, as summarized in Table 2 over the observation period spanning multiple months.

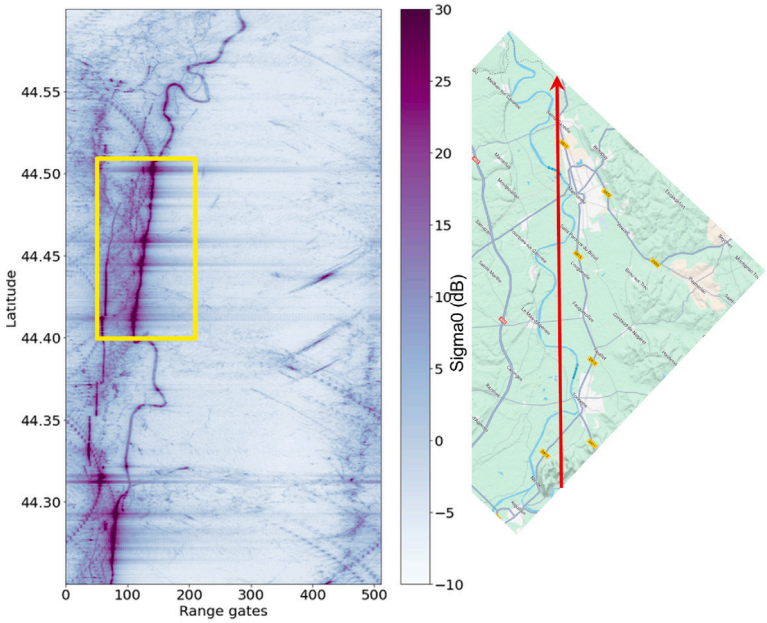

Fig. 4. S6 FFSAR radargram (track 070) observed over the Garonne River. Yellow rectangle shows the studied sector in this paper, between latitude 44.4° and 44.5°. (Background image from © Google Maps.). (For interpretation of the references to color in this figure legend, the reader is referred to the web version of this article.)

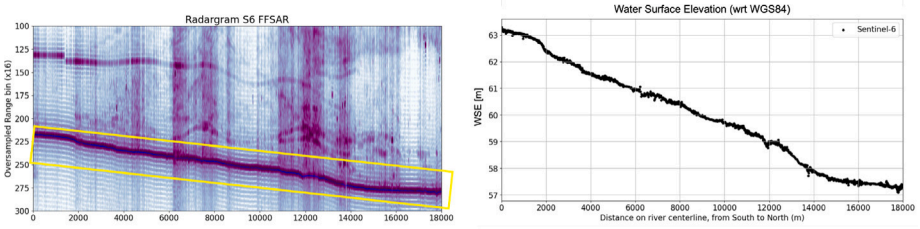

(a) (b)

Fig. 5. (a) S6 FFSAR radargram (on 2022-02-09) with river signal isolation (yellow rectangle). (b) Estimated longitudinal river profile over 18-km-long river segment. (For interpretation of the references to color in this figure legend, the reader is referred to the web version of this article.)

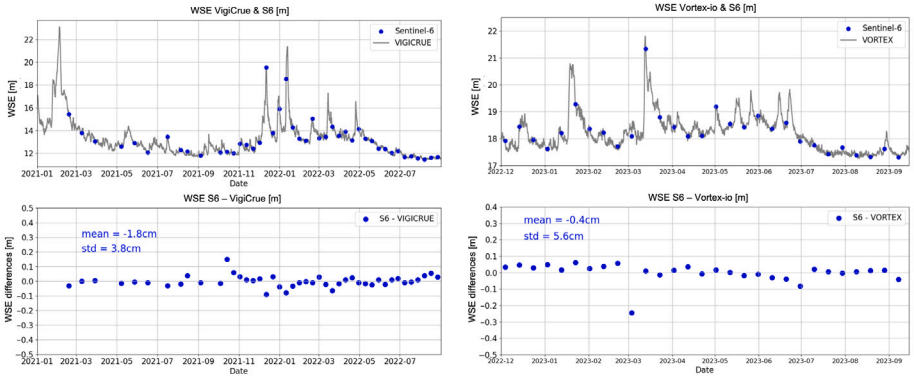

(a) S6 FFSAR vs Marmande VigiCrue station (b) S6 FFSAR vs Mas d'Agenais Vortex-io station

Fig. 6. Comparison between S6-derived WSEs in blue and in-situ WSEs in black.

Table 2
Validation of S6-derived WSEs with respect to in-situ measurements at Marmande (VigiCrue) and Mas d'Agenais (Vortex-io).

Stations	First date	Last date	Number of S6 overpasses	RMSE [cm]
Marmande	2021–02–27	2023-08-28	44	3.8
Mas d'Agenais	2022–12–04	2023-08-28	29	5.5

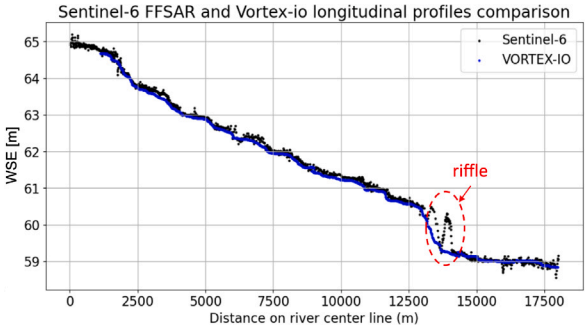

Fig. 7. S6-derived WSE (w.r.t. WGS84) in black over the Garonne River compared to the drone observed profiles in blue on 2022-06-28. (For interpretation of the references to color in this figure legend, the reader is referred to the web version of this article.)

In addition to the in-situ validations, an airborne acquisition campaign was conducted in collaboration with Vortex-io to assess the overall quality of the WSE profile along the observed river segment. A drone equipped with lightweight LiDAR equipment (Vortex-io), offering precise elevations with centimetric accuracy, was deployed for this purpose, in synchronization with the S6 mission overflight on 2022-06-28. Longitudinal WSE profiles obtained from both datasets (from S6 and Vortex-io drone) on 2022-06-28 were compared. S6-derived WSE profile is plotted in black and the drone observed WSE profile is plotted in blue in Fig. 7. With S6 measurements averaging at 100 m showing a precision of 5 cm, an overall bias of merely 5.7 cm was observed between the S6-derived WSE profiles and Vortex-io drone profiles, except at a significant riffle of over one meter (highlighted in red circle). The slight bias can stem from the movement of the river WL during the drone deployment (approximately 2 h) compared to the instantaneous capture by S6. Nonetheless, these assessments collectively underscore the exceptional quality of this processing approach. It is also worth noting that accurate river centerline detection is critical for isolating altimeter signals from the river and the surrounding area (Boy et al., 2023). During high flows, when the water rises and the extents change significantly, the algorithm may misdetect other water surfaces as the river and struggle to obtain precise measurements. Future improvements of this approach can integrate surface water mapping products derived from S1 and S2 images (Peña-Luque et al., 2021).

4. Data assimilation algorithm

4.1. Workflow for the DA algorithm and experimental setup

The general workflow for this study is presented in Fig. 8. The top left boxes describe the hydrometeorological model and hydrologic model providing the upstream forcing $Q(t)$ by ISBA-CTRIP (blue box). The purple box at the center of the schematic represents the T2D model with Ensemble DA involving $N_e = 75$ members. Four experiments were carried out, one in open-loop (OL) mode and three in DA mode. The OL deterministic run is carried out without assimilation, using default parameters and forcing. The first DA experiment involves only in-situ

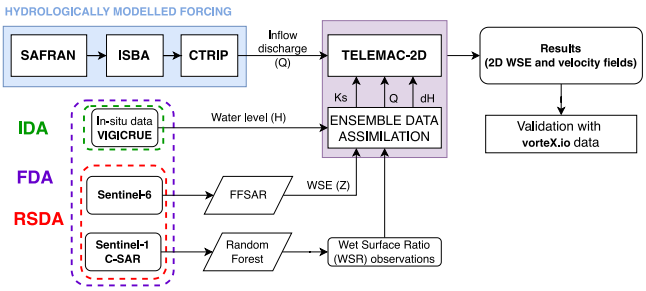

Fig. 8. General workflow for chained modeling and DA.

data assimilation (IDA) as in conventional research works, whereas the second DA experiment assimilates only RS observations (RSDA), and the final DA experiment fully assimilates all available observations (FDA). While IDA benefits from high temporal resolution of in-situ data, enabling the estimation of riverbed parameters that best reflect the dynamics of inflow discharge, RSDA is valuable in ungauged catchments. It helps correct model errors in floodplain areas, where most assets are located. On the other hand, FDA, which assimilates both types of observations, allows for the evaluation of their contributions and complementarity, as well as any potential conflicts in the information provided by each data source. In Fig. 8, the left boxes represent the assimilated data for each experiment: in-situ only (IDA, in green), RS data only from S1 and S6 (RSDA, in red), and all data (FDA, in purple). All four experiments are forced with the upstream BC $Q(t)$ provided by the ISBA-CTRIP discharge (blue line in Fig. 2). In this work, the observed discharge (from the VigiCrue network, orange line in Fig. 2) was not used as forcing data for the experiments; it only serves as a reference to assess the ISBA-CTRIP simulated discharge. The high longitudinal spatial posting rate of S6 data (i.e. a measurement every 10 m along the riverbed) would allow the correction of the riverbed's friction coefficients that could have become necessary in the absence of in-situ data. On the other hand, the large spatial coverage of S1 (with a relatively high revisit frequency, compared to other RS platforms) over the floodplain allows the δH corrections over these regions, thus better representing the floodplain dynamics.

Configurations for all four experiments are gathered in Table 3. The control vector, denoted by $\mathbf{x}$, for the sequential DA experiments accounts, at most, for errors in friction coefficients in the riverbed and the floodplain K_{s_k} (with $k \in [0,6]$), in the upstream forcing through the multiplicative μ and the time shift γ correction to $Q_{prior}(t)$, and the additive term δH_k (with $k \in [1,5]$) to the WL simulated in subdomains of the floodplain. As such, the EnKF DA algorithm involves a control vector $\mathbf{x}$ of dimension up to $n = 14$. IDA only allows for a correction on friction and prior inflow discharge, whereas both RSDA and FDA also correct WL in the floodplain. A cycled EnKF with 18-hour sliding assimilation windows, with 6-hour overlap between two consecutive windows, was implemented for the DA experiments.

The DA is sequentially implemented over each cycle c, during which $n_{obs,c}$ observations are assimilated. Throughout a single cycle, the friction coefficients (K_{s_k} with $k \in [0,6]$), the discharge multiplicative and time shift coefficients (μ and γ, respectively) remain constant, yet they vary between different DA cycles. In contrast, the water level corrections δH_k (with $k \in [1,5]$) are applied over each floodplain subdomain with Incremental Analysis Updating scheme (Bloom et al., 1996) to smooth out temporal discontinuities. The observation errors associated with the in-situ WL and S6 WSE observations are set proportional to their values (i.e. 15%), whereas the observation error associated with the WSR observations is prescribed as a fixed scalar value. The standard deviation of the S1-derived WSR observations for each window c is set between 0.1 and 0.2, depending on the timing of the S1 observation within each assimilation window. A more detailed description of the cycling is given in Nguyen et al. (2023b).

Table 3
Experimental settings.

Name of the experiment	Assimilated observations	Ensemble size N_e	Control vector $\mathbf{x}$	Control vector size n
OL	No assimilation	1	–	0
IDA	In-situ WL	75	$K_{s_{[0:6]}}, \mu, \gamma$	9
RSDA	S1 WSR, and S6 WSE	75	$K_{s_{[0:6]}}, \mu, \gamma, \delta H_{[1:5]}$	14
FDA	In-situ WL, S1 WSR, and S6 WSE	75	$K_{s_{[0:6]}}, \mu, \gamma, \delta H_{[1:5]}$	14

4.2. Description of the EnKF algorithm

The vectors $\mathbf{x}_c^{f,i}$ and $\mathbf{x}_c^{a,i}$ stand for the forecast and analysis control vectors over a DA cycle c, respectively, for i^{th} member with $i \in [1, N_e]$ within an ensemble of size N_e. The forecast step of the EnKF consists in the propagation of N_e control and model state vectors, i.e. $\mathbf{x}_c^{f,i}$ and $\mathbf{s}_c^{f,i}$ in time. The analysis step of the EnKF updates the control $\mathbf{x}_c^{a,i}$ and the associated model state vector $\mathbf{s}_c^{a,i}$.

In the forecast step, the background hydraulic state for each member $\mathbf{s}_c^{f,i}$ results from the integration of the hydrodynamic model $\mathcal{M}_c$: $\mathbb{R}^n \rightarrow \mathbb{R}^m$ from the control space (of dimension n) to the model state (of dimension m) over cycle c:

$$\mathbf{s}_c^{f,i} = \mathcal{M}_c\left(\mathbf{s}_{c-1}^{a,i}, \mathbf{x}_c^{f,i}\right), \tag{1}$$

where $\mathbf{s}_{c-1}^{a,i}$ is the hydraulic state resulting from the analysis at previous cycle $c-1$. In addition, a three-hour spin-up is integrated preceding each cycle c, to equilibrate the model's hydraulic state with the analyzed set of parameters at the beginning of c.

The observation vector $\mathbf{y}_c^o$ for cycle c gathers all in-situ WL, S6 WSE and S1-derived WSR observations. To implement a stochastic EnKF algorithm (Asch et al., 2016), a perturbation ϵ_c is added on $\mathbf{y}_c^o$ to generate an ensemble of N_e observations $\mathbf{y}_c^{o,i}$ for each cycle c. The observation error $\epsilon_c \sim \mathcal{N}(\mathbf{0}, \mathbf{R}_c)$, where $\mathbf{R}_c = \sigma_{obs}^2 \mathbf{I}_{n_{obs}}$ is the observation error covariance matrix. Given the observation errors are assumed to be uncorrelated Gaussians, $\mathbf{R}_c$ is thus diagonal and of standard deviation σ_{obs}. The model equivalent in the observation space, denoted by $\mathbf{y}_c^{f,i}$ with $i \in N_e$, is computed from the background hydraulic state $\mathbf{s}_c^{f,i}$ using the observation operator $\mathcal{H}_c$: $\mathbb{R}^m \rightarrow \mathbb{R}^{n_{obs}}$ from the model state space (of dimension m) to the observation space (of dimension n_{obs}). $\mathcal{H}_c$ extracts/interpolates model outputs at times and locations of the observation vector $\mathbf{y}_c^o$:

$$\mathbf{y}_c^{f,i} = \mathcal{H}_c\left(\mathbf{s}_c^{f,i}\right). \tag{2}$$

Next, the EnKF analysis step updates the control $\mathbf{x}_c^{a,i}$ and the associated model state vector $\mathbf{s}_c^{a,i}$ in an anamorphosed space (Nguyen et al., 2023b,c) using the transformed observation operator $\tilde{\mathcal{H}}_c$, thanks to the Kalman gain $\mathbf{K}_c$ and the innovation vector (between the perturbed observation vector and its model equivalent) over cycle c:

$$\mathbf{x}_c^{a,i} = \mathbf{x}_c^{f,i} + \mathbf{K}_c\left(\tilde{\mathbf{y}}_c^{o,i} - \tilde{\mathbf{y}}_c^{f,i}\right). \tag{3}$$

$\mathbf{K}_c$ is computed from covariance matrices that are stochastically estimated within the ensemble, considering anamorphosed observation vectors $\tilde{\mathbf{y}}^{f,i}$:

$$\mathbf{K}_c = \mathbf{P}_c^{\mathbf{x},\tilde{\mathbf{y}}}\left[\mathbf{P}_c^{\tilde{\mathbf{y}},\tilde{\mathbf{y}}} + \mathbf{R}_c\right]^{-1}. \tag{4}$$

The covariance matrix between the error in the control vector $\mathbf{x}_c^f$ and the error in $\tilde{\mathbf{y}}_c^f$ is denoted by $\mathbf{P}_c^{\mathbf{x},\tilde{\mathbf{y}}}$, whereas the covariance matrix of the error in the background state equivalent in the transformed observation space $\tilde{\mathbf{y}}_c^f$ is $\mathbf{P}_c^{\tilde{\mathbf{y}},\tilde{\mathbf{y}}}$.

Similar to Eq. (1), the hydraulic state $\mathbf{s}_c^{a,i}$, associated with each analyzed control vector $\mathbf{x}_c^{a,i}$, results from the integration of the hydrodynamic model $\mathcal{M}_c$ with the updated parameters:

$$\mathbf{s}_c^{a,i} = \mathcal{M}_c\left(\mathbf{s}_{c-1}^{a,i}, \mathbf{x}_c^{a,i}\right), \tag{5}$$

where $\mathbf{x}_c^{a,i}$ gathers $(K_{s_k})_c^{a,i}$ with $k \in [0,6]$, $\mu_c^{a,i}, \gamma_c^{a,i}$, and $\delta H_k^{a,i}$ with $k \in [1,5]$ over cycle c. It should be noted that the ensemble mean $\overline{\delta H_k^a}$ is used in place of $\delta H_k^{a,i}$ in order to guarantee a smooth WL field.

5. Experimental results

The simulation results were comprehensively assessed with 1D and 2D metrics with respect to the observations. Section 5.1 shows the results of the DA experiments in the control space, whereas those in the observation space are described in Section 5.2. Throughout the following plots, the in-situ observations are plotted in dashed black lines, OL is plotted in blue, IDA is in green, RSDA in red, and FDA in purple. The 1D assessment metrics include the RMSEs computed with respect to in-situ WL time-series at the observing stations, as well as with respect to the S6 WSE time-series along the river centerline. The 2D assessment metric is the Critical Success Index (CSI) computed over the 2D domain with respect to S1-derived flood extent maps. The CSI varies from 0 %, i.e. when there is no common area between the simulated and the observed flood extents, to 100 %, i.e. when the simulated flood extent perfectly fits the observed flood extent.

5.1. Results in the control space

The analyzed parameters from the three DA experiments (IDA, RSDA, and FDA) are shown over time in Fig. 9. The black horizontal dashed lines represent the default values (Table 1) which are used in the OL experiment, whereas the orange, green, and purple curves show the evolution of the controlled parameters over time in IDA, RSDA, and FDA, respectively. For the friction coefficients and the multiplicative factor μ, the background and analysis standard deviations are also displayed around the mean analyzed values. It is worth noting that the standard deviations are not shown for the water level corrections in the floodplain subdomains, for the sake of simplicity. Vertical lines represent the overpass times of the S1 (green/gray vertical dashed–dotted lines) and S6 (cyan dotted lines).

The panels on the left column in Fig. 9 depict the friction coefficients in the floodplain K_{s_0} and in the riverbed K_{s_k} with $k \in [1,6]$. These are corrected over every DA cycle for IDA and FDA. However, the correction occurs at a reduced frequency for RSDA that only assimilates RS data. Indeed, in cases where no observations are available, the control vector would remain unchanged and retain its last analyzed values. On the other hand, the assimilation of in-situ data (in IDA and FDA) leads to significant variability of K_{s_k} (with $k \in [0,6]$) from the default values with a large variance between $[20, 75]$ $\text{m}^{1/3}\ \text{s}^{-1}$. This large variability could be explained by equifinality. In order to reduce this equifinality, we could consider only one stickler zone between two in-situ observations. It appears that friction only affects the water volume in the floodplain during bank overflowing and that the impact of the friction coefficients in the riverbed on flood extent is limited. It is thus difficult to infer a consistent friction value in the riverbed from RS-derived flood extent images.

The first to fifth panels on the right column in Fig. 9 reveal the hydraulic state corrections δH_k with $k \in [1,5]$. They are mostly negative in all five floodplain subdomains. This is attributed to the fact that the event under study is only experiencing mild overflow, except at the flood peak on 2022-01-12. Indeed, the observed flood extent maps derived from the S1 images reveal minimal to no water detected in the floodplain. Therefore, as the model tends to overestimate the flood, DA responds by yielding negative δH in order to empty the floodplain. This also partly reflects the limitations of the hydraulic model, which is currently being improved through the use of

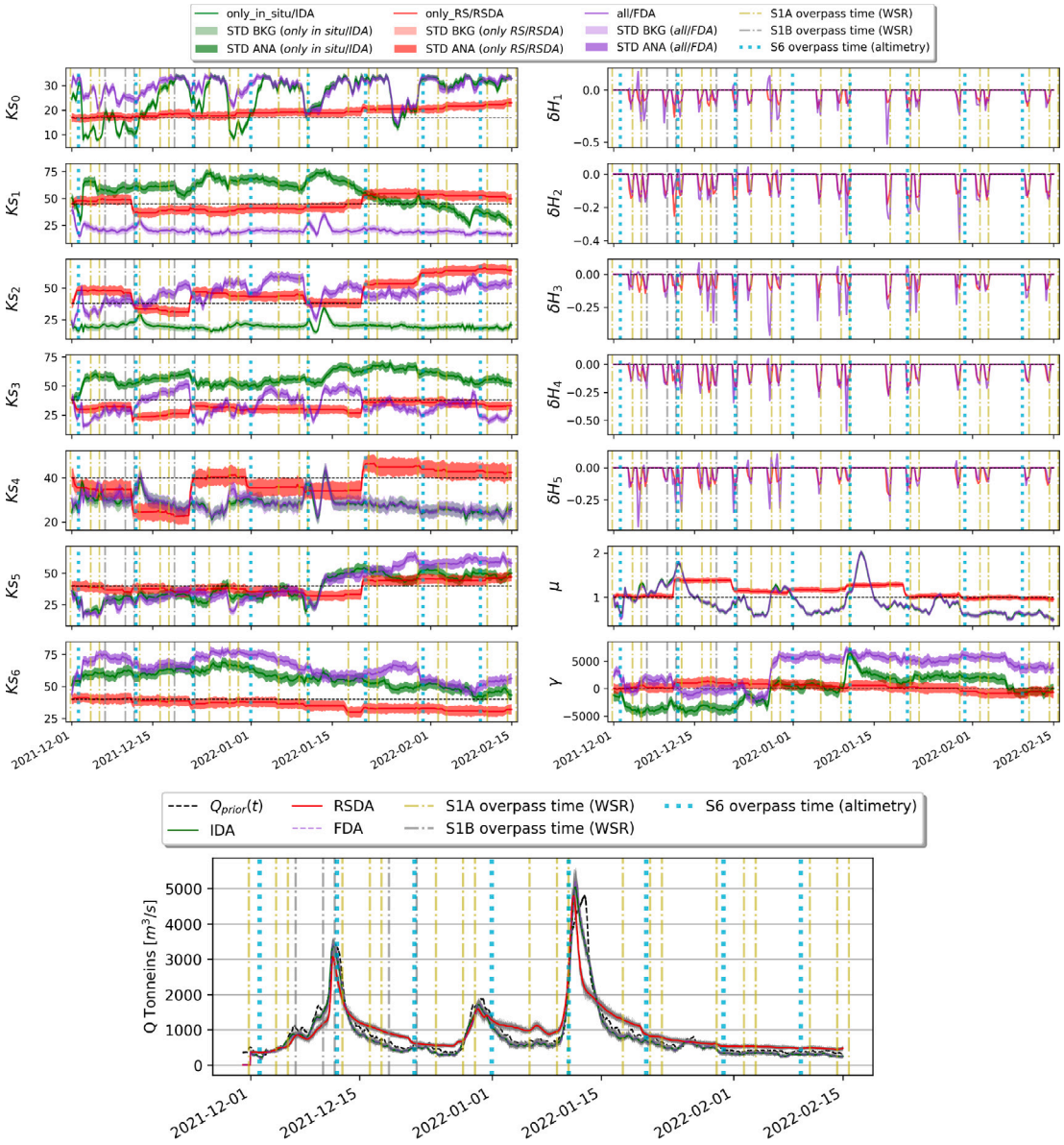

Fig. 9. Evolution over time of the controlled parameters: friction coefficients, water level correction in the floodplain, multiplicative and time shift correction to the inflow, as well as reconstructed inflow, for IDA (green), RSDA (red), FDA (purple). The default parameter values are indicated as black dashed lines. The S6 (respectively, S-1A/-1B) overpass times are indicated in cyan (respectively, green/gray) vertical lines. (For interpretation of the references to color in this figure legend, the reader is referred to the web version of this article.)

a higher-quality DEM and calibration with additional in-situ gauging stations (Sadki et al., 2024). The sixth and seventh panels on the right column show the multiplicative factor μ [dimensionless] and time shift correction γ [seconds] obtained from the analyses. In IDA and FDA, μ and γ fluctuate considerably due to a potential equifinality issue with the large correction in the friction coefficients. In RSDA, where the corrections in friction are smaller, μ remains slightly greater than one and γ is close to zero. In all three DA experiments, μ is greater than one during the high-flow periods, to account for the underestimation in the ISBA-TRIP forcing.

The last panel in Fig. 9 shows the reconstructed upstream inflow discharge with DA, i.e., the ISBA-CTRIP discharge multiplied by the analyzed factor μ and shifted by γ (in seconds) resulting from each of the three DA experiments, and compared with the observed discharge (black-dashed line). The reconstructed upstream inflow discharges by each member of the ensembles, using $\mu_c^{f,i}$ and $\gamma_c^{f,i}$ (within background control vector $\mathbf{x}_c^{f,i}$), are shown in gray. Zoomed-in plots are shown in Fig. B.14 which can be found in Appendix B. The assimilation of either in-situ data (IDA) or S6-derived WSE along the river centerline (RSDA), or both (FDA) leads to the improvement of simulated flood peaks. The analyzed forcing reaches the observed maximum, yet a slight phase delay remains, especially for the third peak. It should be noted that the evaluation of the DA experiments in the control space, for a real event, does not provide a quantitative assessment of the DA performance, because the true values of the control vector are unknown.

5.2. Results in the observation space

5.2.1. Assessment against WLs at observing stations

Table 4 summarizes the root-mean-square errors (RMSE) between the WLs simulated for the studied 2021–2022 flood event by the

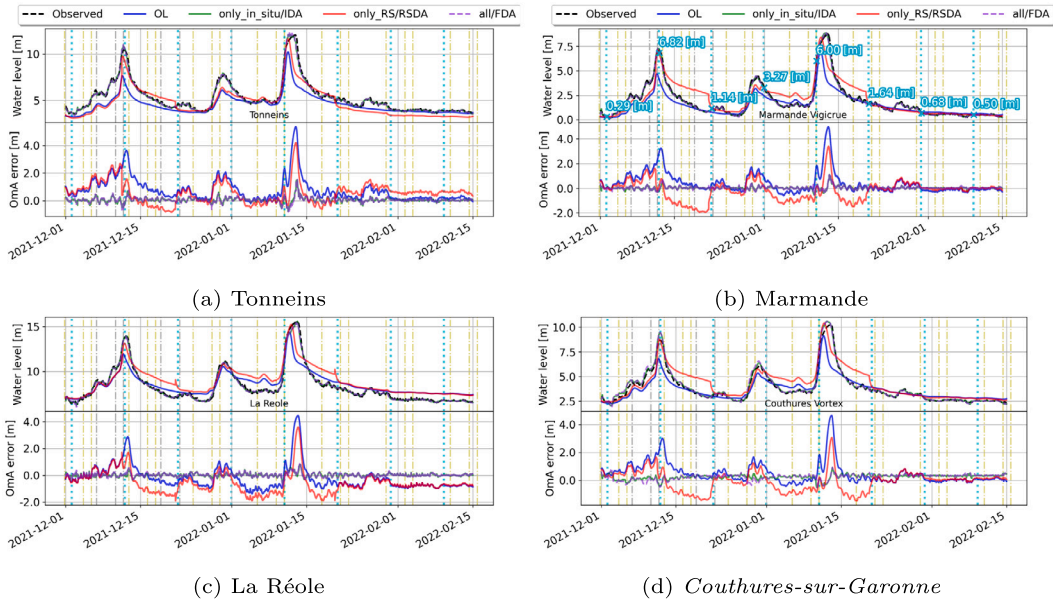

(a) Tonneins (b) Marmande

(c) La Réole (d) *Couthures-sur-Garonne*

Fig. 10. WLs at Tonneins, Marmande, La Réole (analysis, top panels and bottom-left panel), and *Couthures* (*validation*, bottom-right panel). OL is plotted in blue, IDA in green, RSDA in red and FDA in purple. (For interpretation of the references to color in this figure legend, the reader is referred to the web version of this article.)

Table 4
Root-mean-square errors [m] of simulated WL with respect to in-situ measurements at observing stations.

RMSE [m]	Tonneins	Marmande	La Réole	*Couthures*
OL	1.168	0.946	0.945	*0.686*
IDA	0.188	0.135	0.138	*0.168*
RSDA	0.959	0.838	1.014	*0.800*
FDA	0.199	0.144	0.155	*0.196*

experiments OL, IDA, RSDA, and FDA with respect to the observed WLs at observing stations.

Fig. 10 illustrates the WLs simulated for all four experiments, at Tonneins (Fig. 10(a)), Marmande (Fig. 10(b)), La Réole (Fig. 10(c)) where observations are assimilated in the DA experiments, as well as at Couthures (Fig. 10(d)) where observations are used for validation only. The observed WLs time-series are plotted with black-dashed lines. The color codes for OL and DA experiments are similar to those previously described. At all four stations, the WLs simulated by IDA (green) are almost visually identical to those by FDA (purple). In particular, Fig. 10(b) shows the WLs observed by S6 in cyan over the location close to Marmande at S6 overpass times. It should be noted that the S6-derived WSEs are in good agreement with in-situ WSEs at Marmande over the eight overpass time; as indicated in Table 2, the RMSE between in-situ and S6-derived WSE at Marmande over two years is less than 4 cm.

These results demonstrate that the assimilation of the frequent (i.e., of high temporal sampling) in-situ WLs significantly improves the hydraulic state at the observing stations in IDA and FDA. The RMSE for WL at Marmande (computed with respect to in-situ measurements) is improved from 94.6 cm for OL to 13.7 cm for IDA (similar result for FDA, i.e. 15 cm). Similar improvements are observed at Tonneins and La Réole with a reduction in RMSE, from nearly 1 m for OL to less than 20 cm for IDA and FDA. Additionally, the WLs in IDA and FDA show improvements at Couthures, where the in-situ Vortex.io measurements are used for validation only. Although the improvement at Couthures is less significant compared to those at Marmande, IDA and FDA outperform OL, indicating that assimilating VigiCrue observations at Tonneins, Marmande and La Réole allows for coherent WLs with respect to Vortex.io observations at Couthures. The low RSMEs resulting from the DA analysis at Couthures for IDA is likely attributed to its location in the same friction zone as Marmande, thereby benefiting from the correction in the friction coefficient K_{s_4}.

For RSDA, with the contribution of RS data, the overall RMSEs are shown to be noticeable primarily at Tonneins (by 25 % compared to OL), and to a lesser extent at Marmande and Couthures (by 12.3% and 18 %, respectively). These reductions are notably less pronounced compared to those achieved with IDA or FDA. Indeed, the improvement mostly occurs at high-flow periods when S6 data are available. This limited improvement stems from a number of reasons. First, it is worth noting that the S1-derived flood extent maps offer limited knowledge on the flow dynamics in the floodplain since they only observed the flood event at relatively mild flow days. The information in RS observations thus mostly comes from the S6 data. Second, after the assimilation of data from an S6 pass, the analyzed controlled parameters are kept constant over the following cycles, as no RS data are available (or informative) in between. It is thus possible for a correction of WL (typically positive in the case where DA aims at accounting for an underestimated peak in OL based on S6 observations) to remain mistakenly too high until another S6 pass, leading to artificial large correction over time. This advocates for a higher density RS observing network, especially beyond the S6 revisit time of 10 days. It is expected that, for more significant flood events, S1 observations would provide meaningful information, thus densifying the relevant observing network as shown in Nguyen et al. (2022b, 2023c). This also advocates for more frequent and shorter cycling of the DA with a relaxation to default values in between cycles where no observations are available.

5.2.2. *Assessment against S6-derived WSEs along the river centerline*

Fig. 11 illustrates WSE profiles along the river centerline at all S6 overpass times during the simulated period, over the river segment that was observed by the satellite. The curvilinear abscissa of the plots aligns with the flow direction, meaning that smaller abscissa values are found upstream of greater ones. Its zero point is located at Tonneins. High flow conditions were observed on 2021-12-12 (first peak), 2021-12-31 (slightly after the second peak) and 2022-01-10 (slightly before

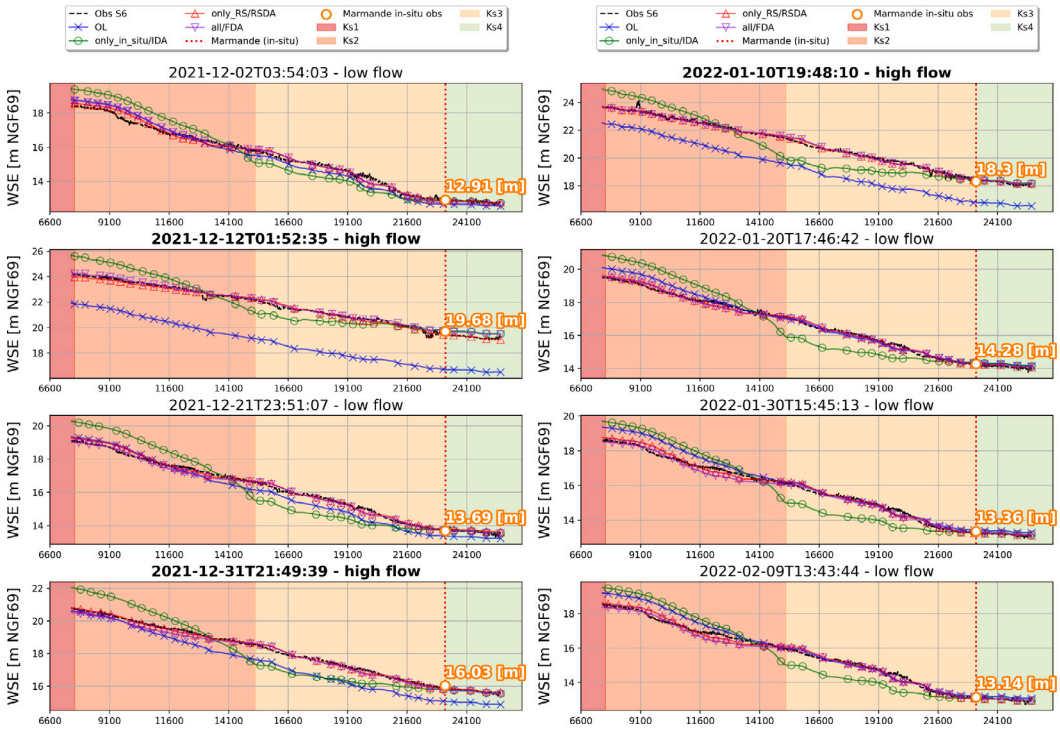

Fig. 11. WSE profile along river centerline between S6-derived observations (black-dashed line) and from the experiments. The curvilinear abscissa's zero point is located at Tonneins. OL is plotted in blue, IDA in green, RSDA in red and FDA in purple. (For interpretation of the references to color in this figure legend, the reader is referred to the web version of this article.)

Table 5
RMSE [m] of simulated WSE along the river centerline with respect to S6 WSE measurements. High-flow dates are marked with †.

RMSE [m]	2021–12–02 03:54:03	*2021-12-12 01:52:35*†	2021–12–21 23:51:07	*2021-12-31 21:49:39*†	*2022-01-10 19:48:10*†	2022–01–20 17:46:42	2022-01-30 15:45:13	2022–02–09 13:43:44	Avg.
OL	0.336	2.810	0.391	0.771	1.667	0.316	0.432	0.399	0.890
IDA	0.678	0.751	0.806	0.799	0.829	0.875	0.805	0.732	0.784
RSDA	0.177	0.146	0.143	0.095	0.120	0.124	0.163	0.154	0.140
FDA	0.244	0.167	0.142	0.186	0.129	0.127	0.182	0.175	0.169

the third peak). The S6-derived WSE profiles are represented by black-dashed lines, while the OL-, IDA-, RSDA-, and FDA-simulated WSE profiles are respectively plotted in blue, orange, green, and purple lines. The WSE values of the in-situ observation at Marmande are indicated in orange. The different riverbed friction zones are represented as shaded areas in the plot background for K_{s_k} with $k \in [1,4]$. They follow the same color codes as in Fig. 1. The RMSEs computed between the simulated WSEs and S6 observations are provided in Table 5, with high-flow dates are found in column 3, 5, and 6. Another version of Fig. 11 including the ensemble members for the DA experiments can be found in Appendix B.

The spatial density of S6 observations with FFSAR processing allows for a spatial correction of the hydraulic state along the river. First, it should be noted that S6-derived WSEs are in good agreement with the in-situ WSEs at Marmande (orange numbers showing in-situ WSE along vertical, orange-dotted line), as previously observed in Fig. 10(b). However, the absence of additional in-situ data upstream of Marmande during the event limits the broader validation of S6-derived observations across this region and timeframe, especially given that the Mas d'Agenais station data (Vortex-io) became available only at the end of 2022.

At low flows, OL (blue lines) tends to slightly overestimate the S6-derived WSEs in the upstream part of the observed river segment (between the curvilinear abscissa 7,500 and 12,500 m), but slightly underestimates the WSEs beyond the middle of the segment. This heterogeneity may be related to the calibration of the friction zones that is only constrained by in-situ observations. At high flows, OL significantly underestimates S6-derived WSE over the entire segment. This underestimation reaches up to 2.81 m at the first high-flow date on 2021-12-12, and 1.67 m on 2021-01-10.

Because the S6-derived observations closely match the in-situ data at Marmande, assimilating the in-situ observations in IDA helps align the simulated WSEs more closely with the S6-derived WSEs at Marmande and surrounding regions (i.e. between the curvilinear abscissa 22,500 and 25,000 m) at all S6 overpass times. Yet, IDA struggles to replicate this for the WSEs in the areas upstream of Marmande (i.e. before the curvilinear abscissa 22,500 m). Table 5 shows that the RMSEs computed between IDA-simulated WSEs and S6-derived WSEs are smaller than those of OL only at two high-flow dates 2021-12-12 and 2022-01-10. Yet, at the other time steps, RMSEs of IDA are larger than those of OL. It is likely that the equifinality in the correction of friction coefficients K_{s_1}, K_{s_2} and K_{s_3} in IDA, leads to unrealistic

WSEs upstream of Marmande, thus inconsistent with S6 measurements. Indeed, Fig. 11 shows that the WSEs of IDA (green lines) are typically overestimated, compared to the S6 observations (black-dashed lines) in the K_{s_2} zone, but underestimated in the K_{s_3} zone by more than 1 m. In the absence of independent in-situ data in this upstream part of the river and given that S6 data were previously validated with respect to drone data (Section 3.3), it appears reasonable to qualify the simulated WSE profile by IDA as unrealistic, prompting caution regarding IDA's dynamics both in the riverbed and across the floodplain.

In both RSDA (red lines) and FDA experiments (purple lines), the simulated WSEs along the river are quite consistent with S6-derived data at all S6 observation times, as opposed to IDA. Therefore, the RMSEs computed with respect to S6 measurements are greatly reduced in RSDA and FDA, with RSDA providing the best results. When comparing IDA and FDA, the spatial density of S6 observations proved crucial. FDA was able to simulate more accurate WSEs by refining local friction coefficients K_{s_1}, K_{s_2} and K_{s_3}. In contrast, IDA, relying only on in-situ data from Marmande (within the observed river segment), could not achieve the same accuracy. FDA presents a compromise between in-situ data and S6 data, and the analysis is brought closer to both sources of data as shown in Fig. 11, and previously in Fig. 10. This demonstrates that the DA strategy succeeds in retrieving controlled parameters and improving the dynamics of the flow thanks to S6 data only over the observed river reach. It is also capable of combining S6 data with in-situ data through the analysis.

It is important to note that such improvement is only possible at S6 observation times (every 10 days) and that the benefits of assimilating S6 data only do not persist over time, as shown by the overestimated WLs at observing stations by RSDA in between two S6 observation times in Fig. 10. An intermediate conclusion is that keeping the latest controlled parameters as background values for the following cycles (over which no RS data are available) leads to poor quality results in RSDA and that this strategy should be revisited for further works.

5.2.3. Assessment against WSRs in the floodplain

Fig. 12 displays the observed WSR (black lines) derived from S1 images and the WSR computed for OL (blue lines), IDA (green lines), RSDA (red lines), and FDA (purple lines) experiments at S1 overpass times within the five floodplain subdomains.

First, it is worth noting that the flood extent maps derived from S1 SAR images depict minimal water surfaces within the floodplain, due to S1's reduced revisit frequency after December 2021 and the missed flood peak. Indeed, the timing of S1 image acquisition coincided with periods of relatively low flow, compounded by the malfunction of one of the two S1 satellites (S-1B, shown by gray dash-dotted vertical line in Fig. 3) became defective just prior to the third peak. This reduced the S1 observation capacity by a half after mid-December 2021. Therefore, the observed WSRs shown in Fig. 12 (black lines) are almost zeros throughout the flood event. As OL tends to underestimate the flood due to the weak forcing discharge from ISBA-CTRIP, WSRs simulated by OL are nearly zero, closely resembling the observed WSRs.

The assimilation of in-situ data only in IDA presents much larger WSRs than the observed ones, meaning that IDA leads to overflooding. This confirms the limitation in IDA which was also found in our previous works (Nguyen et al., 2022b, 2023b) and the doubts mentioned above regarding IDA's dynamics: while it succeeds in retrieving WLs that approach the in-situ observations at observing stations, the assimilation of in-situ data only, leads to an overestimation of the flooding. The overflow occurs at the beginning of the simulation period over the fourth and fifth subdomains; it appears after the flood peak and maintains during the recess for the first and third subdomains.

The assimilation of the RS data by RSDA and FDA yields WSRs that are more coherent with the flood extents derived from S1 images, especially in the third and fifth subdomains. The simulated WSRs within the fourth subdomain remain overestimated over the entire event in spite of the state correction. Over the fifth subdomain, FDA must accommodate in-situ data that leads to overflooding (as in IDA). This demands more effort from FDA, and thus larger δH_5 corrections compared to those by RSDA, to remove water in this area as shown in Fig. 9.

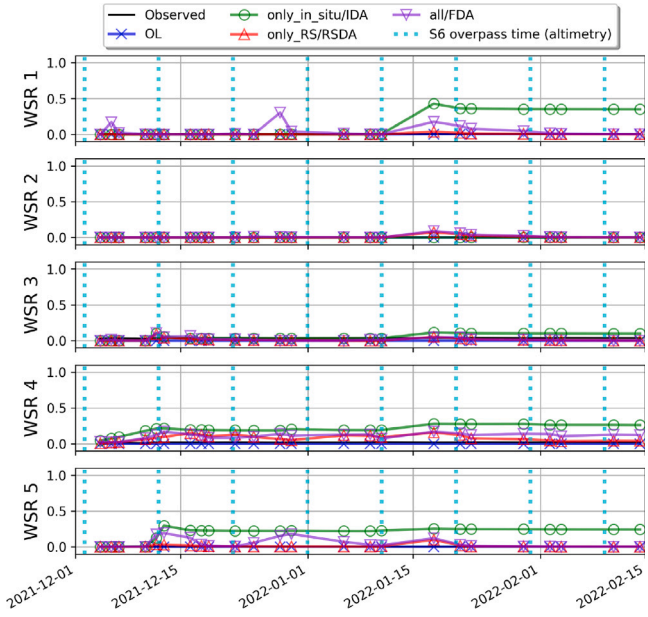

Fig. 12. Simulated and observed WSR values in the five floodplain zones. OL is plotted in blue, IDA in green, RSDA in red and FDA in purple. (For interpretation of the references to color in this figure legend, the reader is referred to the web version of this article.)

5.2.4. 2D validation with contingency maps and CSI scores

Fig. 13 displays the contingency maps for all experiments, computed with respect to the observed S1-derived flood extent maps (first column). Two specific regions are omitted from the 2D assessments; first in the first meander due to numerical flooding imposed by the upstream boundary condition in the hydrodynamic model; second near La Réole where the model topography is known to be uncertain. They are shown in red-hatched regions in Fig. 13. The contingency maps show one out of four outcomes for each pixel. When the model and observation are in agreement, the pixel is indicated in blue: light blue when non-flooded and dark blue for flooded pixels. Observed wet pixels incorrectly predicted as non-flooded (i.e. underprediction) are represented in yellow, whereas observed dry pixels incorrectly predicted as flooded (i.e. overprediction) are shown in red. The contingency maps are shown at the first high-flow date (2021-12-11 19:00 and 2021-12-12 19:00), before the flood peak (2022-01-10 19:00), and during the recess (2022-01-21 07:00). It is worth noting that S6 observation on 2021-12-12 01:52:35 occurred in between the two S1 observations of the first peak.

Because of the satellite overpass times, S1 fails to observe flooding for the studied event. Consequently, OL, which underestimates the dynamics of whole flood event due to weak ISBA-CTRIP inflow discharge, yields a high agreement with the observed flood extent maps. As such, OL (second column) outperforms all the DA experiments in terms of 2D assessments. Yet, this does not imply that OL is the best experiment, as previously shown. The third column shows the contingency maps for IDA, which shows overprediction areas (red pixels) at all four dates within the first, fourth and fifth subdomains (i.e. δH_1, δH_4, and δH_5, respectively), and underprediction areas (yellow pixels) within the third subdomain δH_3.

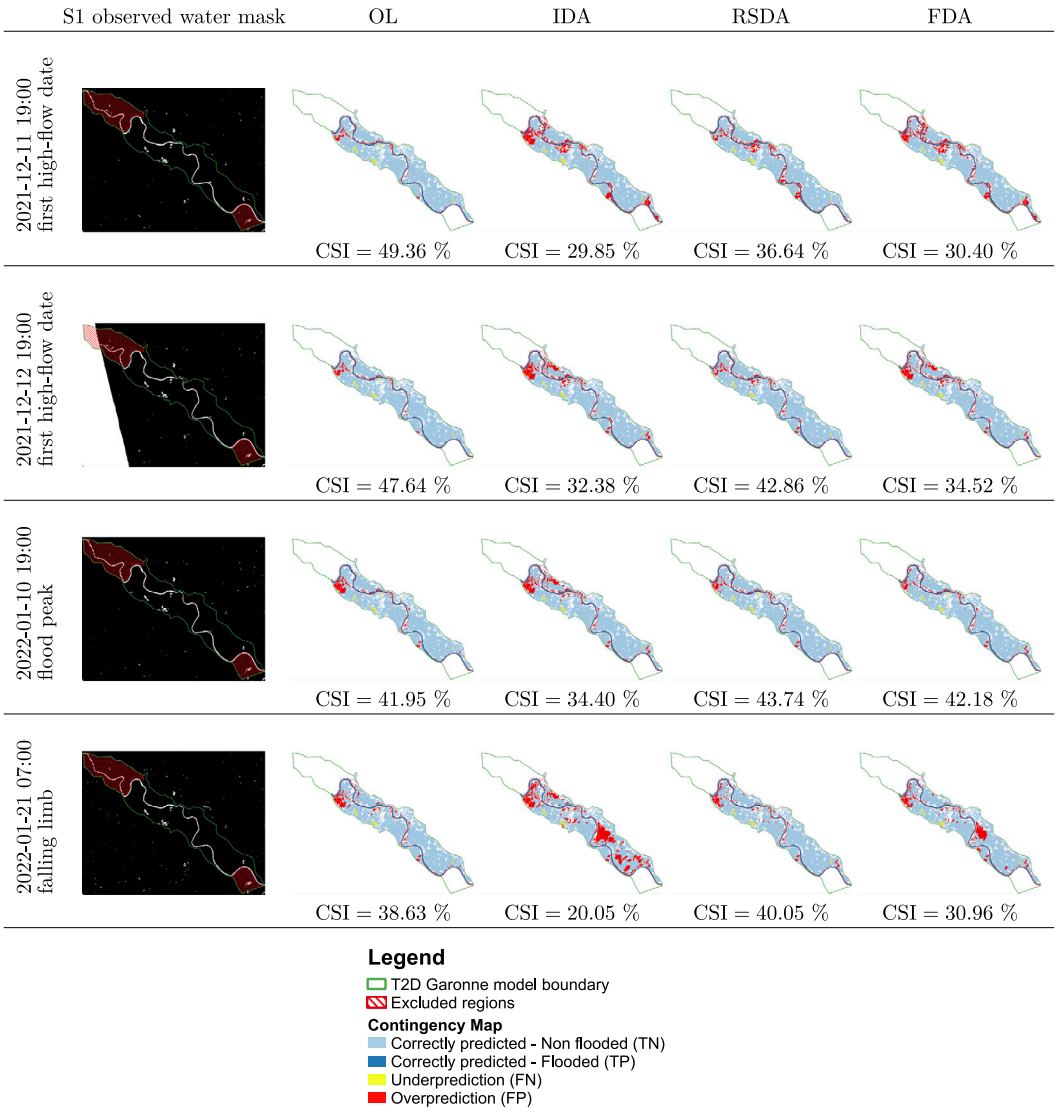

Fig. 13. Contingency maps of OL, IDA, RSDA, and FDA with respect to S1-derived flood extents.

The assimilation of S1-derived WSR allows RSDA (fourth column) to reduce the overprediction areas and improve the overall CSI on all four dates, compared to IDA. It should be noted that the assimilation of the S6 observation on 2021-12-12 01:52:35 significantly decreases the overprediction between the two S1 images at 2021-12-11 19:00 and 2021-12-12 19:00. This stems from the reduction of friction in the riverbed (K_{s_1} to K_{s_4}), as shown in Fig. 9 by the RSDA (red line).

6. Conclusion and perspectives

This paper presents the merits of assimilating Sentinel-6-Michael Freilich altimetry data, and 2D flood extent observations derived from Sentinel-1 SAR images, in hindcast mode. The DA was performed with an Ensemble Kalman Filter implemented upon a local hydrodynamic TELEMAC-2D model, forced by the large-scale hydrologic ISBA-CTRIP model. Previous works (Nguyen et al., 2022b, 2023b) have shown that the assimilation of heterogeneous data from in-situ and RS observations allows an effective correction of errors in observed forcing, friction and model. These findings remain valid when the local hydrodynamic model is forced with discharge simulated by a large-scale hydrologic model. The use of in-situ data is essential as the characteristics of the in-situ network (dense in time but sparse in space) complement that of the remote-sensing observations (sparse in time and dense in space). Flood extent information from S1 SAR images is expressed in terms of Wet Surface Ratio computed over selected floodplain subdomains, whereas the altimetry data from S6 nadir and off-nadir observations are processed with FFSAR, to provide dense WSE measurements, every 10 m, along the river centerline every 10 days. This study represents an innovative study to utilize S6 altimetry data in river and fluvial flood hydrodynamics. It focused on the Garonne Marmandaise catchment, particularly on the flood event from December 2021 to February 2022, during which both types of satellite observations were available. The S6 observations covered the upstream half of the studied Garonne River reach. Four experiments were conducted: one in open-loop (OL) mode and three others in DA mode assimilating, in-situ observations only (IDA), remote-sensing observations only (RSDA) or both (FDA), using a dual state-parameter EnKF (Nguyen et al., 2022b). The control vector included friction and hydrological forcing corrections, augmented with corrections of the hydraulic state in floodplain subdomains. DA was applied sequentially over an 18-hour sliding window with 6-hour overlap. The results were comprehensively assessed with 1D and

2D metrics with respect to assimilated data and independent data whenever available.

It has been demonstrated that the OL simulation significantly underestimates the WL in the riverbed and the extent of flooding, due to the significant underestimation of upstream discharge provided by ISBA-CTRIP, especially during high flow periods. In IDA and FDA, the assimilation of in-situ WLs data notably enhances the flow dynamics in the riverbed compared to OL, thereby reducing errors in the ISBA-CTRIP forcing. However, the assimilation of remote-sensing observations alone in RSDA improves WLs at observing stations, compared to OL, at RS observation times (as shown in Fig. 10); yet the results deteriorate in periods between RS observations. This suggests that without in-situ data, it is nearly impossible to compensate for large errors in the discharge, given the low revisit frequency of the satellites. Alternative EnKF cycling strategies should be investigated, for instance, by relaxing the analysis values back to the default values (i.e. Table 1) to avoid over-corrections between cycles when only a few observations are available.

The poor coherence of the longitudinal WSE profile in IDA when compared to S6 observations (considered as independent references for IDA), is conjectured to originate from equifinality issues associated with corrections made to friction coefficients and forcing data. It was also shown that IDA overestimates the flooding and yields large WSR misfits, as the in-situ WL observations measured by the river do not provide any relevant information on the dynamics in the floodplain. The assimilation of both in-situ and RS observations in FDA alleviates the equifinality and provides significant enhancements in WLs both at observing stations and along the observed river segment, particularly when high spatial resolution S6-derived WSE measurements are available. The merits and limitations of assimilating RS observations were also assessed with 2D metrics computed with respect to S1-derived flood extents. Despite poorly informative S1-derived flood extent maps, regarding high-flow periods, the dynamics of RSDA and FDA in the floodplain are better than that of IDA.

This article demonstrates the added value from S6 altimetry data for river hydrodynamics. However, it is important to acknowledge that the used technique, employing FFSAR, is only applicable under specific conditions. While effective in certain situations like that of the Garonne Marmandaise, it has inherent limitations. The accuracy of the river centerline is crucial for isolating altimeter signals from rivers. During flood events, when the riverbed and water extent undergo substantial changes, the algorithm may struggle to extract precise measurements, potentially leading to significant errors. Further investigation and validation with independent data, both during low and high flow conditions, are necessary to address this issue. S6 provides a dense WSE profile along the river center line, allowing for the description of water surface elevation away from in-situ observing stations. Such a beneficial feature is also expected for the large-swath altimetry satellite SWOT, which provides WSEs in both the river and floodplain. However, a limitation lies in the temporal coverage of the satellite, which may be insufficient to capture the dynamics of medium-sized rivers like the Garonne adequately. Nevertheless, this research lays the groundwork for future utilization of data from the constellation of altimeters, such as the upcoming SMASH mission (Blumstein et al., 2019). Since the present research work focused on the multi-source DA strategy in the hindcast mode, its forecast capability is limited to the next DA cycle. To fully understand the influence of DA corrections, it is important to assess their performance in a full forecasting mode, exploring different lead times that extend beyond the hydraulic network's propagation time.

This study highlights the significance of enhancing the temporal and spatial density of the observing network using RS data to improve the representation of flow dynamics in floodplains through numerical models employing advanced DA strategies. Furthermore, it emphasizes the critical role of in-situ data, particularly in addressing high levels of uncertainty in forcing data provided by large-scale hydrologic models. Ultimately, this research work advocates for a multi-source DA strategy implemented on a chained hydrologic-hydrodynamic model, effectively leveraging diverse Earth Observation data. Such a combination of models and observations, aimed at developing new observing strategies, paves the way for a Digital Twin framework in hydrology.

CRediT authorship contribution statement

Thanh Huy Nguyen: Writing – review & editing, Writing – original draft, Visualization, Validation, Software, Methodology, Investigation, Formal analysis, Data curation, Conceptualization. **Sophie Ricci:** Writing – review & editing, Writing – original draft, Validation, Supervision, Resources, Project administration, Methodology, Funding acquisition, Formal analysis, Conceptualization. **François Boy:** Writing – review & editing, Writing – original draft, Visualization, Validation, Methodology, Investigation, Data curation. **Andrea Piacentini:** Visualization, Validation, Software, Methodology, Formal analysis, Conceptualization. **Simon Munier:** Validation, Methodology, Investigation, Data curation. **Santiago Peña Luque:** Project administration. **Christophe Fatras:** Software, Data curation. **Ludovic Cassan:** Writing – review & editing, Validation, Supervision, Resources, Project administration . **Raquel Rodriguez Suquet:** Supervision, Resources, Project administration, Funding acquisition.

Declaration of competing interest

The authors declare that they have no known competing financial interests or personal relationships that could have appeared to influence the work reported in this paper.

Acknowledgments

This research was part of the SWIFT project funded by the Fonds National de la Recherche (FNR), Luxembourg (Grant no. INTER/ANR/23/17800438) and by the Agence Nationale de la Recherche (ANR), France (Grant no. ANR-23-CE56-0009). The authors express their gratitude to Electricité de France (EDF) for supplying the TELEMAC-2D model for the Garonne Marmandaise catchment, as well as to SCHAPI, SPCs Garonne-Tarn-Lot, and Gironde-Adour-Dordogne for providing in-situ data. Additionally, they thank Vortex-io for providing the drone data, as well as J.-C. Poisson and V. Fouqueau (Vortex-io) for their assistance and advice regarding altimetric reference.

Appendix A. Radar altimeters

Radar altimeters operate in several different spectral bands with respect to their mission objectives, as well as having different spatial resolution (i.e., along-track sampling and inter-track distances) and temporal resolution depending on the satellite orbit (Łyszkowicz and Bernatowicz, 2017), as summarized by Table A.6.

Table A.6
Summary of radar altimetry satellites characteristics.

Altimetry satellite	Spectral band	Years in operation	Revisit frequency	Cross-track separation
ERS-1	Ku	1991–2000	35 days	80 km
ERS-2	Ku	1995–2011	35 days	80 km
ENVISAT	S/Ku	2002–2012	35 days	80 km
SARAL/ALtiKa	Ka	2013–	35 days	80 km
TOPEX/Poseidon	C/Ku	1992–2005	10 days	315 km
Jason-1	C/Ku	2001–2013	10 days	315 km
Jason-2/OSTM	C/Ku	2008–2019	10 days	315 km
Jason-3	C/Ku	2016–	10 days	315 km
Sentinel-6MF	C/Ku	2020-	10 days	315 km
CryoSat-2	Ku	2010–	369 days	7 km
Sentinel-3A/B	C/Ku	2016/2018-	27 days	52 km
SWOT	Ka	2022–	21 days	137.26 km

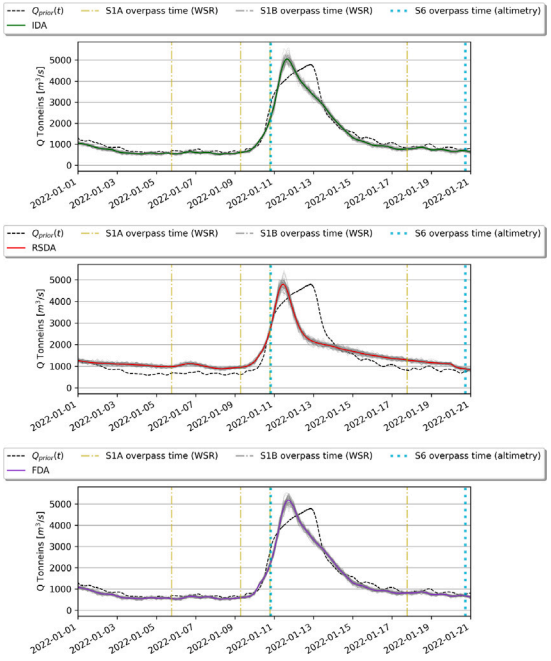

Fig. B.14. Evolution over time of the reconstructed inflow, for IDA (green), RSDA (red), FDA (purple), between 2022-01-01 and 2022-01-20. The S6 (respectively, S-1A/-1B) overpass times are indicated in cyan (respectively, green/gray) vertical lines. (For interpretation of the references to color in this figure legend, the reader is referred to the web version of this article.)

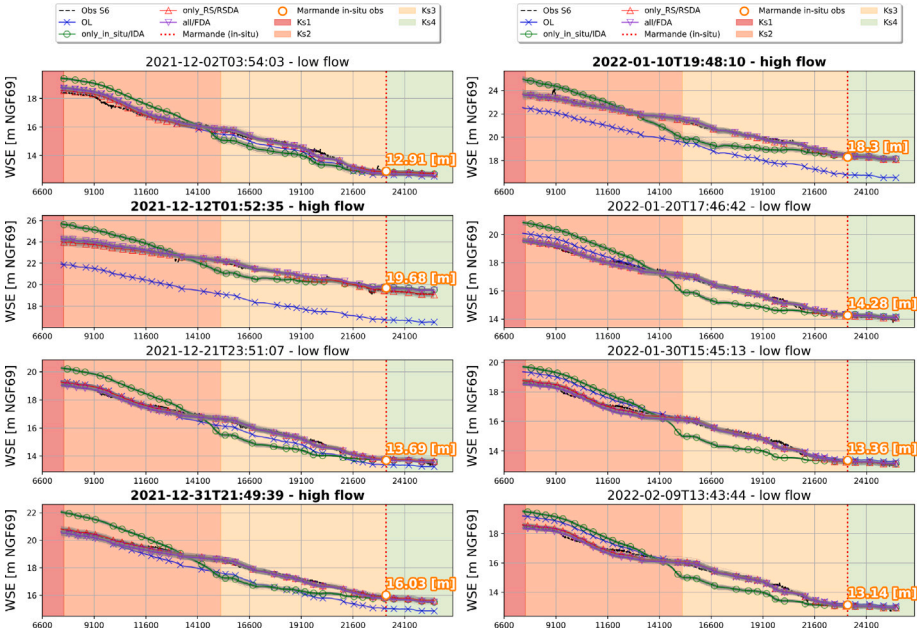

Fig. B.15. WSE profile along river centerline between S6-derived observations (black-dashed line) and from the experiments. The curvilinear abscissa's zero point is located at Tonneins. OL is plotted in blue, IDA in green, RSDA in red and FDA in purple. Member WSEs are shown in gray. (For interpretation of the references to color in this figure legend, the reader is referred to the web version of this article.)

Appendix B. Additional figures

See Figs. B.14 and B.15.

Appendix C. Data and software resource

See Table C.7.

Table C.7
Data and software resource.

Tools/Data	Access link
TELEMAC-2D	Homepage (https://www.opentelemac.org/)
ISBA-CTRIP	Homepage (https://www.umr-cnrm.fr/spip.php?article1092&lang=en)
VigiCrue in-situ data	HydroPortail (https://hydro.eaufrance.fr/)
Sentinel-1 data	Alaska Satellite Facility Vertex (https://search.asf.alaska.edu/) Copernicus Data Space Ecosystem (https://browser.dataspace.copernicus.eu/)
Flood extent mapping	FloodML (https://github.com/CNES/floodml)
Sentinel-6 data	NASA Earthdata Search (https://search.earthdata.nasa.gov) EUMETSAT User Portal (https://user.eumetsat.int/catalogue)
FFSAR	SMAP (https://github.com/cls-obsnadir-dev/SMAP-FFSAR) for Sentinel-3. An alternative algorithm similar to the one used in this study can be found in Ehlers et al. (2025).

Data availability

The authors do not have permission to share data.

References

Adeel, Z., Alarcón, A.M., Bakkensen, L., Franco, E., Garfin, G.M., McPherson, R.A., Méndez, K., Roudaut, M.B., Saffari, H., Wen, X., 2020. Developing a comprehensive methodology for evaluating economic impacts of floods in Canada, Mexico and the United States. Int. J. Disaster Risk Reduct. 50, 101861. http://dx.doi.org/10.1016/j.ijdrr.2020.101861.

Andreadis, K.M., Schumann, G.J., 2014. Estimating the impact of satellite observations on the predictability of large-scale hydraulic models. Adv. Water Resour. 73, 44–54. http://dx.doi.org/10.1016/j.advwatres.2014.06.006.

Annis, A., Nardi, F., 2019. Integrating VGI and 2D hydraulic models into a data assimilation framework for real time flood forecasting and mapping. Geo-Spatial Inf. Sci. 22 (4), 223–236. http://dx.doi.org/10.1080/10095020.2019.1626135.

Annis, A., Nardi, F., Castelli, F., 2022. Simultaneous assimilation of water levels from river gauges and satellite flood maps for near-real-time flood mapping. Hydrol. Earth Syst. Sci. 26 (4), 1019–1041, [Online]. Available: https://hess.copernicus.org/articles/26/1019/2022/.

Asch, M., Bocquet, M., Nodet, M., 2016. Data Assimilation: Methods, Algorithms, and Applications. SIAM, http://dx.doi.org/10.1137/1.9781611974546.

Bates, P.D., De Roo, A., 2000. A simple raster-based model for flood inundation simulation. J. Hydrol. 236 (1–2), 54–77. http://dx.doi.org/10.1016/S0022-1694(00)00278-X.

Begg, C., 2018. Power, responsibility and justice: a review of local stakeholder participation in European flood risk management. Local Environ. 23 (4), 383–397. http://dx.doi.org/10.1080/13549839.2017.1422119.

Besnard, A., Goutal, N., 2011. Comparaison de modèles 1D à casiers et 2D pour la modélisation hydraulique d'une plaine d'inondation–Cas de la Garonne entre Tonneins et La Réole. Houille Blanche (3), 42–47, https://doi.org/10.1051/lhb/2011031.

Biancamaria, S., Frappart, F., Leleu, A.-S., Marieu, V., Blumstein, D., Desjonquères, J.-D., Boy, F., Sottolichio, A., Valle-Levinson, A., 2017. Satellite radar altimetry water elevations performance over a 200 m wide river: Evaluation over the Garonne river. Adv. Space Res. 59 (1), 128–146. http://dx.doi.org/10.1016/j.asr.2016.10.008.

Bloom, S., Takacs, L., Da Silva, A., Ledvina, D., 1996. Data assimilation using incremental analysis updates. Mon. Weather Rev. 124 (6), 1256–1271. http://dx.doi.org/10.1175/1520-0493(1996)124<1256:DAUIAU>2.0.CO;2.

Blöschl, G., Hall, J., Viglione, A., Perdigão, R.A., Parajka, J., Merz, B., Lun, D., Arheimer, B., Aronica, G.T., Bilibashi, A., et al., 2019. Changing climate both increases and decreases European river floods. Nature 573 (7772), 108–111. http://dx.doi.org/10.1038/s41586-019-1495-6.

Blumstein, D., Biancamaria, S., Guérin, A., Maisongrande, P., 2019. A Potential Constellation of Small Altimetry Satellites Dedicated to Continental Surface Waters (SMASH Mission). In: AGU Fall Meeting Abstracts, vol. 2019, pp. H43N–2257.

Boergens, E., Buhl, S., Dettmering, D., Klüppelberg, C., Seitz, F., 2017. Combination of multi-mission altimetry data along the Mekong River with spatio-temporal kriging. J. Geod. 91, 519–534. http://dx.doi.org/10.1007/s00190-016-0980-z.

Bogning, S., Frappart, F., Blarel, F., Niño, F., Mahé, G., Bricquet, J.-P., Seyler, F., Onguéné, R., Etamé, J., Paiz, M.-C., et al., 2018. Monitoring water levels and discharges using radar altimetry in an ungauged river basin: The case of the Ogooué. Remote. Sens. 10 (2), 350. http://dx.doi.org/10.3390/rs10020350.

Boulange, J., Hanasaki, N., Yamazaki, D., Pokhrel, Y., 2021. Role of dams in reducing global flood exposure under climate change. Nat. Commun. 12 (1), 417. http://dx.doi.org/10.1038/s41467-020-20704-0.

Boy, F., Poisson, J.-C., Fouqueau, V., Picot, N., Le Gac, S., 2023. Measuring longitudinal river profiles from Sentinel-6 fully-focused SAR mode. In: 2023 Ocean Surface Topography Science Team (OSTST) Meeting. p. 96.

Brêda, J., Paiva, R., Bravo, J., Passaia, O., Moreira, D., 2019. Assimilation of satellite altimetry data for effective river bathymetry. Water Resour. Res. 55 (9), 7441–7463. http://dx.doi.org/10.1029/2018WR024010.

Chang, C.-H., Lee, H., Hossain, F., Basnayake, S., Jayasinghe, S., Chishtie, F., Saah, D., Yu, H., Sothea, K., Du Bui, D., 2019. A model-aided satellite-altimetry-based flood forecasting system for the Mekong River. Environ. Model. Softw. 112, 112–127. http://dx.doi.org/10.1016/j.envsoft.2018.11.017.

Da Silva, J.S., Calmant, S., Seyler, F., Rotunno Filho, O.C., Cochonneau, G., Mansur, W.J., 2010. Water levels in the amazon basin derived from the ERS 2 and ENVISAT radar altimetry missions. Remote Sens. Environ. 114 (10), 2160–2181. http://dx.doi.org/10.1016/j.rse.2010.04.020.

Dasgupta, A., Hostache, R., Ramsankaran, R., Schumann, G.J.-P., Grimaldi, S., Pauwels, V.R.N., Walker, J.P., 2021. A mutual information-based likelihood function for particle filter flood extent assimilation. Water Resour. Res. 57 (2), http://dx.doi.org/10.1029/2020WR027859, e2020WR027859.

Decharme, B., Alkama, R., Papa, F., Faroux, S., Douville, H., Prigent, C., 2012. Global off-line evaluation of the ISBA-TRIP flood model. Clim. Dyn. 38, 1389–1412. http://dx.doi.org/10.1007/s00382-011-1054-9.

Decharme, B., Delire, C., Minvielle, M., Colin, J., Vergnes, J.-P., Alias, A., Saint-Martin, D., Séférian, R., Sénési, S., Voldoire, A., 2019. Recent changes in the ISBA-CTRIP land surface system for use in the CNRM-CM6 climate model and in global off-line hydrological applications. J. Adv. Model. Earth Syst. 11 (5), 1207–1252. http://dx.doi.org/10.1029/2018MS001545.

Di Mauro, C., Hostache, R., Matgen, P., Pelich, R., Chini, M., Jan van Leeuwen, P., Nichols, N., Bloschl, G., 2021. Assimilation of probabilistic flood maps from SAR data into a coupled hydrologic-hydraulic forecasting model: a proof of concept. Hydrol. Earth Syst. Sci. 25, 4081–4097. http://dx.doi.org/10.5194/hess-25-4081-2021.

Dinardo, S., Maraldi, C., Cadier, E., Rieu, P., Aublanc, J., Guerou, A., Boy, F., Moreau, T., Picot, N., Scharroo, R., 2024. Sentinel-6 MF poseidon-4 radar altimeter: Main scientific results from S6PP LRM and UF-SAR chains in the first year of the mission. Adv. Space Res. 73 (1), 337–375, [Online]. Available: https://www.sciencedirect.com/science/article/pii/S0273117723005641.

Domeneghetti, A., 2016. On the use of SRTM and altimetry data for flood modeling in data-sparse regions. Water Resour. Res. 52 (4), 2901–2918. http://dx.doi.org/10.1002/2015WR017967.

Donlon, C.J., Cullen, R., Giulicchi, L., Vuilleumier, P., Francis, C.R., Kuschnerus, M., Simpson, W., Bouridah, A., Caleno, M., Bertoni, R., Rancaño, J., Pourier, E., Hyslop, A., Mulcahy, J., Knockaert, R., Hunter, C., Webb, A., Fornari, M., Vaze, P., Brown, S., Willis, J., Desai, S., Desjonqueres, J.-D., Scharroo, R., Martin-Puig, C., Leuliette, E., Egido, A., Smith, W.H., Bonnefond, P., Le Gac, S., Picot, N., Tavernier, G., 2021. The copernicus Sentinel-6 mission: Enhanced continuity of satellite sea level measurements from space. Remote Sens. Environ. 258, 112395, [Online]. Available: https://www.sciencedirect.com/science/article/pii/S0034425721001139.

Durand, M., Gleason, C.J., Pavelsky, T.M., Prata de Moraes Frasson, R., Turmon, M., David, C.H., Altenau, E.H., Tebaldi, N., Larnier, K., Monnier, J., et al., 2023. A framework for estimating global river discharge from the Surface Water and Ocean Topography satellite mission. Water Resour. Res. 59 (4), http://dx.doi.org/10.1029/2021WR031614, e2021WR031614.

Egido, A., Smith, W.H., 2016. Fully focused SAR altimetry: Theory and applications. IEEE Trans. Geosci. Remote Sens. 55 (1), 392–406. http://dx.doi.org/10.1109/TGRS.2016.2607122.

Ehlers, F., Slobbe, C., Schlembach, F., Kleinherenbrink, M., Verlaan, M., 2025. Polygon-Informed Cross-Track Altimetry (PICTA): Estimating river water level profiles with the sentinel-6 altimeter. Remote Sens. Environ. 316, 114479, [Online]. Available: https://www.sciencedirect.com/science/article/pii/S0034425724005054.

Ehlers, F., Slobbe, C., Verlaan, M., Kleinherenbrink, M., 2024. Looking beyond nadir: Measuring densely sampled river elevation profiles with the sentinel-6 altimeter. In: EGU General Assembly Conference Abstracts. p. 8949.

El Garroussi, S., de Lozzo, M., Ricci, S., Lucor, D., Goutal, N., Goeury, C., Boyaval, S., 2019. Uncertainty quantification in a two-dimensional river hydraulic model. In: International Conference on Uncertainty Quantification in Computational Sciences and Engineering.

El Garroussi, S., Ricci, S., De Lozzo, M., Goutal, N., Lucor, D., 2022. Tackling random fields non-linearities with unsupervised clustering of polynomial chaos expansion in latent space: application to global sensitivity analysis of river flooding. Stoch. Environ. Res. Risk Assess. 36 (3), 693–718. http://dx.doi.org/10.1007/s00477-021-02060-7.

Fenicia, F., Kavetski, D., Savenije, H.H., 2011. Elements of a flexible approach for conceptual hydrological modeling: 1. Motivation and theoretical development. Water Resour. Res. 47 (11), http://dx.doi.org/10.1029/2010WR010174.

García-Pintado, J., Mason, D.C., Dance, S.L., Cloke, H.L., Neal, J.C., Freer, J., Bates, P.D., 2015. Satellite-supported flood forecasting in river networks: A real case study. J. Hydrol. 523, 706–724. http://dx.doi.org/10.1016/j.jhydrol.2015.01.084.

García-Pintado, J., Neal, J.C., Mason, D.C., Dance, S.L., Bates, P.D., 2013. Scheduling satellite-based SAR acquisition for sequential assimilation of water level observations into flood modelling. J. Hydrol. 495, 252–266. http://dx.doi.org/10.1016/j.jhydrol.2013.03.050.

Giustarini, L., Hostache, R., Kavetski, D., Chini, M., Corato, G., Schlaffer, S., Matgen, P., 2016. Probabilistic flood mapping using synthetic aperture radar data. IEEE Trans. Geosci. Remote Sens. 54 (12), 6958–6969. http://dx.doi.org/10.1109/TGRS.2016.2592951.

Giustarini, L., Matgen, P., Hostache, R., Montanari, M., Plaza, D., Pauwels, V., De Lannoy, G., Keyser, R.D., Pfister, L., Hoffmann, L., et al., 2011. Assimilating SAR-derived water level data into a hydraulic model: a case study. Hydrol. Earth Syst. Sci. 15 (7), 2349–2365. http://dx.doi.org/10.5194/hess-15-2349-2011.

Gómez Olivé, A., Gibert, F., Garcia-Mondéjar, A., McKeown, C., 2023. Water Extent Measurements with Sentinel-6 Fully - Focused SAR data. In: EGU General Assembly Conference Abstracts. pp. EGU–448.

Grimaldi, S., Li, Y., Pauwels, V.R., Walker, J.P., 2016. Remote sensing-derived water extent and level to constrain hydraulic flood forecasting models: Opportunities and challenges. Surv. Geophys. 37 (5), 977–1034. http://dx.doi.org/10.1007/s10712-016-9378-y.

Hervouet, J.-M., 2007. Hydrodynamics of Free Surface Flows: Modelling with the Finite Element Method, vol. 360, Wiley Online Library, http://dx.doi.org/10.1002/9780470319628.

Hostache, R., Chini, M., Giustarini, L., Neal, J., Kavetski, D., Wood, M., Corato, G., Pelich, R.-M., Matgen, P., 2018. Near-real-time assimilation of SAR-derived flood maps for improving flood forecasts. Water Resour. Res. 54 (8), 5516–5535. http://dx.doi.org/10.1029/2017WR022205.

Huang, T., Baillarin, S., Altinok, A., Blanchet, G., Hausman, J., Kettig, P., Shah, S., 2020. Distributed machine learning and data fusion for flood detection and monitoring. In: AGU Fall Meeting Abstracts, vol. 2020, pp. IN041–09.

Jafarzadegan, K., Moradkhani, H., Pappenberger, F., Moftakhari, H., Bates, P., Abbaszadeh, P., Marsooli, R., Ferreira, C., Cloke, H.L., Ogden, F., Duan, Q., 2023. Recent advances and new frontiers in riverine and coastal flood modeling. Rev. Geophys. 61 (2), [Online]. Available: https://agupubs.onlinelibrary.wiley.com/doi/abs/10.1029/2022RG000788, e2022RG000788 2022RG000788.

Jamali, B., Löwe, R., Bach, P.M., Urich, C., Arnbjerg-Nielsen, K., Deletic, A., 2018. A rapid urban flood inundation and damage assessment model. J. Hydrol. 564, 1085–1098. http://dx.doi.org/10.1016/j.jhydrol.2018.07.064.

Jarihani, A.A., Callow, J.N., Johansen, K., Gouweleeuw, B., 2013. Evaluation of multiple satellite altimetry data for studying inland water bodies and river floods. J. Hydrol. 505, 78–90. http://dx.doi.org/10.1016/j.jhydrol.2013.09.010.

Jiang, L., Madsen, H., Bauer-Gottwein, P., 2019. Simultaneous calibration of multiple hydrodynamic model parameters using satellite altimetry observations of water surface elevation in the Songhua River. Remote Sens. Environ. 225, 229–247. http://dx.doi.org/10.1016/j.rse.2019.03.014.

Kettig, P., Baillarin, S., Blanchet, G., Taillan, C., Ricci, S., Nguyen, T.-H., Huang, T., Altinok, A., Chung, N.T., Valladeau, G., Goeury, R., Roumagnac, A., 2021. The SCO-FloodDAM project: New observing strategies for flood detection, alert and rapid mapping. In: 2021 IEEE International Geoscience and Remote Sensing Symposium IGARSS. pp. 1464–1467.

Kleinherenbrink, M., Naeije, M., Slobbe, C., Hoogeboom, P., 2018. Application of fully-focused SAR altimetry to the Wadden Sea. In: AGU Fall Meeting Abstracts, vol. 2018, pp. OS43A–05.

Lai, X., Liang, Q., Yesou, H., Daillet, S., 2014. Variational assimilation of remotely sensed flood extents using a 2-D flood model. Hydrol. Earth Syst. Sci. 18 (11), 4325–4339. http://dx.doi.org/10.5194/hess-18-4325-2014.

Łyszkowicz, A., Bernatowicz, A., 2017. Current state of art of satellite altimetry. Geod. Cartogr. (24), 31–47. http://dx.doi.org/10.1515/geocart-2017-0016.

Martinis, S., Kuenzer, C., Twele, A., 2015. Flood studies using synthetic aperture radar data. In: Remote Sensing Handbook. CRC Press, pp. 145–173. http://dx.doi.org/10.1201/b19321.

Mason, D., Schumann, G.-P., Neal, J., Garcia-Pintado, J., Bates, P., 2012. Automatic near real-time selection of flood water levels from high resolution synthetic aperture radar images for assimilation into hydraulic models: A case study. Remote Sens. Environ. 124, 705–716. http://dx.doi.org/10.1016/j.rse.2012.06.017.

Masson-Delmotte, V., Zhai, P., Pirani, A., Connors, S., Péan, C., Berger, S., Caud, N., Chen, Y., Goldfarb, L., Gomis, M.I., Huang, M., Leitzell, K., Lonnoy, E., matthewes, J.B.R., Maycock, T.K., Waterfield, T., Yelekci, O., Yu, R., Zhou, B. (Eds.), 2021a. IPCC 2021: Climate Change 2021: The physical Science Basis. Contribution of Working Group I to the Sixth Assessment Report of the Intergovernmental Panel on Climate Change. Cambridge Univertisty Press, (in press).

Masson-Delmotte, V., Zhai, P., Pirani, A., Connors, S., Péan, C., Berger, S., Caud, N., Chen, Y., Goldfarb, L., Gomis, M.I., Huang, M., Leitzell, K., Lonnoy, E., matthewes, J.B.R., Maycock, T.K., Waterfield, T., Yelekci, O., Yu, R., Zhou, B. (Eds.), 2021b. IPCC 2021: Summary for Policymakers. In: Climate Change 2021: The physical Science Basis. Contribution of Working Group I to the Sixth Assessment Report of the Intergovernmental Panel on Climate Change. Cambridge Univertisty Press, (in press).

Molina Burgués, R., Gibert, F., Gómez, A., Garcia-Mondéjar, A., Aparici, M.R.i., 2023. Water Surface Height Measurements with Sentinel-6 Fully-Focused SAR Over Inland Targets. In: EGU General Assembly Conference Abstracts. pp. EGU–449.

Moradkhani, H., Sorooshian, S., Gupta, H.V., Houser, P.R., 2005. Dual state–parameter estimation of hydrological models using ensemble Kalman filter. Adv. Water Resour. 28 (2), 135–147. http://dx.doi.org/10.1016/j.advwatres.2004.09.002.

Munier, S., Decharme, B., 2022. River network and hydro-geomorphological parameters at 1/12° resolution for global hydrological and climate studies. Earth Syst. Sci. Data 14 (5), 2239–2258, https://essd.copernicus.org/articles/14/2239/2022/.

Nguyen, T.H., Delmotte, A., Fatras, C., Kettig, P., Piacentini, A., Ricci, S., 2021. Validation and improvement of data assimilation for flood hydrodynamic modelling using SAR imagery data. In: Proceedings of the 27th TELEMAC-MASCARET User Conference October. TUC2020, pp. 100–108.

Nguyen, T.H., Piacentini, A., Ricci, S., Cassan, L., Munier, S., Bonassies, Q., Rodriguez-Suquet, R., 2024. Remote sensing data assimilation with a chained hydrologic-hydraulic model for flood forecasting. arXiv e-prints, arXiv:2405.00567, arXiv:2405.00567.

Nguyen, T.H., Ricci, S., Fatras, C., Piacentini, A., Delmotte, A., Lavergne, E., Kettig, P., 2022a. Improvement of flood extent representation with remote sensing data and data assimilation. IEEE Trans. Geosci. Remote Sens. 60, 1–22. http://dx.doi.org/10.1109/TGRS.2022.3147429.

Nguyen, T.H., Ricci, S., Piacentini, A., Bonassies, Q., Rodriguez Suquet, R., Peña Luque, S., Marlis, K., David, C., 2023a. Reducing uncertainties of a chained hydrologic-hydraulic models to improve flood forecasting using multi-source earth observation data. In: IGARSS 2023-2023 IEEE International Geoscience and Remote Sensing Symposium. IEEE, pp. 1525–1528.

Nguyen, T.H., Ricci, S., Piacentini, A., Fatras, C., Kettig, P., Blanchet, G., Peña Luque, S., Baillarin, S., 2022b. Dual state-parameter assimilation of SAR-derived wet surface ratio for improving fluvial flood reanalysis. Water Resour. Res. 58 (11), [Online]. Available: https://agupubs.onlinelibrary.wiley.com/doi/abs/10.1029/2022WR033155, e2022WR033155 2022WR033155.

Nguyen, T.H., Ricci, S., Piacentini, A., Simon, E., Rodriguez Suquet, R., Pena Luque, S., 2023b. Gaussian anamorphosis for ensemble Kalman filter analysis of SAR-derived wet surface ratio observations. IEEE Trans. Geosci. Remote Sens. 62 (1–21), http://dx.doi.org/10.1109/TGRS.2023.3338296.

Nguyen, T.H., Ricci, S., Piacentini, A., Simon, E., Suquet, R., Peña Luque, S., 2023c. Dealing with non-Gaussianity of SAR-derived wet surface ratio for flood extent representation improvement. In: IGARSS 2023 - 2023 IEEE International Geoscience and Remote Sensing Symposium. pp. 1595–1598.

Noilhan, J., Planton, S., 1989. A simple parameterization of land surface processes for meteorological models. Mon. Weather Rev. 117 (3), 536–549. http://dx.doi.org/10.1175/1520-0493(1989)117<0536:ASPOLS>2.0.CO;2.

Oki, T., Sud, Y., 1998. Design of total runoff integrating pathways (TRIP)—A global river channel network. Earth Interactions 2 (1), 1–37. http://dx.doi.org/10.1175/1087-3562(1998)002<0001:DOTRIP>2.3.CO;2.

Pal, M., 2005. Random forest classifier for remote sensing classification. Int. J. Remote Sens. 26 (1), 217–222. http://dx.doi.org/10.1080/01431160412331269698.

Peña-Luque, S., Ferrant, S., Cordeiro, M.C., Ledauphin, T., Maxant, J., Martinez, J.-M., 2021. Sentinel-1&2 multitemporal water surface detection accuracies, evaluated at regional and reservoirs level. Remote. Sens. 13 (16), 3279. http://dx.doi.org/10.3390/rs13163279.

Pinter, N., Santos, N., Hui, R., 2017. Preliminary Analysis of Hurricane Harvey Flooding in Harris County. Technical Report, Retrieved from UC Davis Center for Watershed Sciences, California WaterBlog, Texas, [Online]. Available: https://californiawaterblog.com/2017/09/01/preliminary-analysis-of-hurricane-harvey-flooding-in-harris-county-texas/.

Rentschler, J., Salhab, M., 2020. People in Harm's Way: Flood Exposure and Poverty in 189 Countries. The World Bank.

Revilla-Romero, B., Wanders, N., Burek, P., Salamon, P., de Roo, A., 2016. Integrating remotely sensed surface water extent into continental scale hydrology. J. Hydrol. 543, 659–670. http://dx.doi.org/10.1016/j.jhydrol.2016.10.041.

Ricci, S., Nguyen, T.H., Le Gac, S., Boy, F., Piacentini, A., Rodriquez-Suquet, R., Peña-Luque, S., Bonassies, Q., Emery, C., 2023. Comparisons and water level analyses using Sentinel-6MF satellite altimetry data with 1D Mascaret and 2D Telemac models. In: EGU General Assembly Conference Abstracts. pp. EGU–6513.

Sadki, M., Cassan, L., Bonassies, Q., Piacentini, A., Nguyen, T.H., Ricci, S., 2024. Mise à jour du modèle T2D Garonne - Apport des nouvelles acquisitions de données. Technical Report, CERFACS - Toulouse, France, [Online]. Available: https://cnrs.hal.science/hal-04749413.

Schumann, G., Giustarini, L., Tarpanelli, A., Jarihani, B., Martinis, S., 2023. Flood modeling and prediction using earth observation data. Surv. Geophys. 44 (5), 1553–1578. http://dx.doi.org/10.1007/s10712-022-09751-y.

Shah, M., Rahman, A., Chowdhury, S., 2018. Challenges for achieving sustainable flood risk management. J. Flood Risk Manag. 11 (S1), S352–S358, [Online]. Available: https://onlinelibrary.wiley.com/doi/abs/10.1111/jfr3.12211.

Sulistioadi, Y., Tseng, K.-H., Shum, C., Hidayat, H., Sumaryono, M., Suhardiman, A., Setiawan, F., Sunarso, S., 2015. Satellite radar altimetry for monitoring small rivers and lakes in Indonesia. Hydrol. Earth Syst. Sci. 19 (1), 341–359. http://dx.doi.org/10.5194/hess-19-341-2015.

The Ad Hoc Group, Vörösmarty, C., Askew, A., Grabs, W., Barry, R., Birkett, C., Döll, P., Goodison, B., Hall, A., Jenne, R., et al., 2001. Global water data: A newly endangered species. Eos, Trans. Am. Geophys. Union 82 (5), 54–58. http://dx.doi.org/10.1029/01EO00031, https://agupubs.onlinelibrary.wiley.com/doi/abs/10.1029/01EO00031.

Torres, R., Snoeij, P., Geudtner, D., Bibby, D., Davidson, M., Attema, E., Potin, P., Rommen, B., Floury, N., Brown, M., et al., 2012. GMES Sentinel-1 mission. Remote Sens. Environ. 120, 9–24. http://dx.doi.org/10.1016/j.rse.2011.05.028.

Tourian, M., Tarpanelli, A., Elmi, O., Qin, T., Brocca, L., Moramarco, T., Sneeuw, N., 2016. Spatiotemporal densification of river water level time series by multimission satellite altimetry. Water Resour. Res. 52 (2), 1140–1159. http://dx.doi.org/10.1002/2015WR017654.

United Nations Office for Disaster Risk Reduction, 2020. The Human Cost of Disasters: an Overview of the Last 20 Years. Technical Report, United Nations Office for Disaster Risk Reduction, [Online]. Available: https://www.undrr.org/publication/human-cost-disasters-overview-last-20-years-2000-2019.

United Nations Office for Disaster Risk Reduction, 2022. Global Assessment Report on Disaster Risk Reduction. Technical Report, United Nations Office for Disaster Risk Reduction, [Online]. Available: https://www.undrr.org/gar2022-our-world-risk#container-downloads.

Wasko, C., Nathan, R., Stein, L., O'Shea, D., 2021. Evidence of shorter more extreme rainfalls and increased flood variability under climate change. J. Hydrol. 603, 126994. http://dx.doi.org/10.1016/j.jhydrol.2021.126994.

Wongchuig-Correa, S., de Paiva, R.C.D., Biancamaria, S., Collischonn, W., 2020. Assimilation of future SWOT-based river elevations, surface extent observations and discharge estimations into uncertain global hydrological models. J. Hydrol. 590, 125473. http://dx.doi.org/10.1016/j.jhydrol.2020.125473.

Zakharova, E., Nielsen, K., Kamenev, G., Kouraev, A., 2020. River discharge estimation from radar altimetry: Assessment of satellite performance, river scales and methods. J. Hydrol. 583, 124561. http://dx.doi.org/10.1016/j.jhydrol.2020.124561.